

Modeling ferrous–ferric iron chemistry with application to martian surface geochemistry

Giles M. Marion ^{a,*}, Jeffrey S. Kargel ^b, David C. Catling ^c

^a Desert Research Institute, 2215 Raggio Parkway, Reno, NV 89512, USA

^b University of Arizona, Tucson, AZ 85721, USA

^c University of Bristol, Bristol BS8 1RJ, England, UK

Received 20 June 2007; accepted in revised form 12 October 2007; available online 23 October 2007

Abstract

The Mars Global Surveyor, Mars Exploration Rover, and Mars Express missions have stimulated considerable thinking about the surficial geochemical evolution of Mars. Among the major recent mission findings are the presence of jarosite (a ferric sulfate salt), which requires formation from an acid-sulfate brine, and the occurrence of hematite and goethite on Mars. Recent ferric iron models have largely focused on 25 °C, which is a major limitation for models exploring the geochemical history of cold bodies such as Mars. Until recently, our work on low-temperature iron-bearing brines involved ferrous but not ferric iron, also obviously a limitation. The objectives of this work were to (1) add ferric iron chemistry to an existing ferrous iron model (FREZCHEM), (2) extend this ferrous/ferric iron geochemical model to lower temperatures (<0 °C), and (3) use the reformulated model to explore ferrous/ferric iron chemistries on Mars.

The FREZCHEM model is an equilibrium chemical thermodynamic model parameterized for concentrated electrolyte solutions using the Pitzer approach for the temperature range from <−70 to 25 °C and the pressure range from 1 to 1000 bars. Ferric chloride and sulfate mineral parameterizations were based, in part, on experimental data. Ferric oxide/hydroxide mineral parameterizations were based exclusively on Gibbs free energy and enthalpy data. New iron parameterizations added 23 new ferrous/ferric minerals to the model for this Na–K–Mg–Ca–Fe(II)–Fe(III)–H–Cl–SO₄–NO₃–OH–HCO₃–CO₃–CO₂–O₂–CH₄–H₂O system.

The model was used to develop paragenetic sequences for Rio Tinto waters on Earth and a hypothetical Martian brine derived from acid weathering of basaltic minerals. In general, model simulations were in agreement with field evidence on Earth and Mars in predicting precipitation of stable iron minerals such as jarosites, goethite, and hematite. In addition, paragenetic simulations for Mars suggest that other iron minerals such as lepidocrocite, schwertmannite, ferricopiapite, copiapite, and bilinite may also be present on the surface of Mars. Evaporation or freezing of the Martian brine led to similar mineral precipitates. However, in freezing, compared to evaporation, the following key differences were found: (1) magnesium sulfates had higher hydration states; (2) there was greater total aqueous sulfate (SO_{4T} = SO₄ + HSO₄) removal; and (3) there was a significantly higher aqueous Cl/SO_{4T} ratio in the residual Na–Mg–Cl brine. Given the similarities of model results to observations, alternating dry/wet and freeze/thaw cycles and brine migration could have played major roles in vug formation, Cl stratification, and hematite concretion formation on Mars.

© 2007 Elsevier Ltd. All rights reserved.

1. INTRODUCTION

* Corresponding author. Fax: +1 775 673 7485.
E-mail address: giles.marion@dri.edu (G.M. Marion).

The Mars Global Surveyor, Mars Exploration Rover, and Mars Express missions have stimulated considerable

thinking about the surficial geochemical evolution of Mars and the links between aqueous chemical weathering and mineral precipitation with paleoclimatic evolution (Lane et al., 2004; Kargel, 2004a,b; Morris et al., 2004, 2006; Squyres et al., 2004, 2006; Bibring et al., 2005, 2006; Clark et al., 2005; Gendrin et al., 2005; Glotch and Christensen, 2005; Langevin et al., 2005; McLennan et al., 2005; Navrotsky et al., 2005; Tosca et al., 2005; Tosca and McLennan, 2006; McSween, 2006; Ming et al., 2006; Glotch and Rogers, 2007). Less than a decade ago, some prevailing models of Martian evaporite geochemistry emphasized carbonate mineralization (e.g., Catling, 1999; Morse and Marion, 1999), but this perspective, like so much else about our thinking about Mars, was upended by the twin definitive results in recent years that carbonates are exceedingly rare on Mars and minerals indicative of acidic conditions are locally abundant and perhaps widespread. These conditions destroy carbonates, and, in sulfur-rich environments, produce sulfates, which have been found to be abundant and widespread and to form locally massive accumulations (Squyres et al., 2004, 2006; Gendrin et al., 2005; Catling et al., 2006; Glotch and Rogers, 2007).

Among the major recent mission findings are the presence of the mineral jarosite (a ferric sulfate salt), which requires formation from an acid-sulfate brine (Bishop et al., 2004; Klingelhöfer et al., 2004; Kargel, 2004b; Kargel and Marion, 2004; Clark et al., 2005; Golden et al., 2005; Navrotsky et al., 2005; Tosca et al., 2005; Fernandez-Remolar et al., in press), and the occurrence of hematite and goethite on Mars (Christensen et al., 2001, 2004; Bandfield, 2002; Morris et al., 2004, 2006; Squyres et al., 2004, 2006; Ming et al., 2006; Klingelhöfer et al., 2004; McSween, 2006). Especially intriguing are occurrences of these ferric sulfates and oxides in intimate association with each other and with other sulfate minerals (Squyres et al., 2004, 2006; Glotch and Rogers, 2007), suggesting that either the ferric sulfates and oxides formed together or, more likely, the iron-bearing sulfates have incompletely transformed to the oxides.

It is thus apparent that much about Martian surface and upper crustal geochemistry involves iron-rich, acidic sulfate brines, a point predicted two decades ago by Burns (1987). Recent ferric iron models have largely focused on 25 °C (Drouet and Navrotsky, 2003; Christov, 2004; King et al., 2004; Majzlan et al., 2004; Tosca et al., 2005; Tosca and McLennan, 2006), which is a major limitation for models exploring the geochemical history of cold bodies such as Mars. Until recently, our work on low-temperature iron-bearing brines involved ferrous but not ferric iron (Marion et al., 2003), also obviously a limitation.

The objectives of this work were to (1) add ferric iron chemistry to an existing ferrous iron model (FREZCHEM), (2) extend this ferrous/ferric iron geochemical model to lower temperatures (<0 °C), and (3) use the reformulated model to explore ferrous/ferric iron chemistries on Mars.

2. METHODS AND MATERIALS

2.1. FREZCHEM Model

The FREZCHEM model is an equilibrium chemical thermodynamic model parameterized for concentrated electrolyte solutions using the Pitzer approach (Pitzer, 1991, 1995) for the temperature range from <-70 to 25 °C and the pressure range from 1 to 1000 bars (Marion and Farren, 1999; Marion, 2001, 2002; Marion et al., 2003, 2005, 2006a,b,c; Marion and Kargel, in press). The previous version of the model had been parameterized for the Na–K–Mg–Ca–Fe(II)–H–Cl–SO₄–NO₃–OH–HCO₃–CO₃–CO₂–O₂–CH₄–H₂O system and included 58 solid phases including ice, 11 chloride minerals, 14 sulfate minerals, 15 carbonate minerals, five solid-phase acids, three nitrate minerals, six acid-salts, one iron oxide and two gas hydrates. An objective of this work was to develop a ferrous/ferric iron model based on classical chemical thermodynamic principles that can be incorporated seamlessly into the FREZCHEM model. This involved the incorporation of 23 new ferrous/ferric iron solid phases into the FREZCHEM model. A FORTRAN version of the resulting iron model is available from the Senior Author (giles.marion@dri.edu).

2.2. Pitzer approach

In the Pitzer approach, the activity coefficients (γ) as a function of temperature at 1.01 bar pressure for cations (M), anions (X), and neutral aqueous species (N), such as CO₂(aq) or CH₄(aq), are given by

$$\begin{aligned} \ln(\gamma_M) = & z_M^2 F + \sum m_a (2B_{Ma} + ZC_{Ma}) \\ & + \sum m_c (2\Phi_{Mc} + \sum m_a \Psi_{Mca}) + \sum \sum m_a m_a' \Psi_{Ma a'} \\ & + z_M \sum \sum m_c m_a C_{ca} \\ & + 2 \sum m_n \lambda_{nM} + \sum \sum m_n m_a \zeta_{nMa} \end{aligned} \quad (1)$$

$$\begin{aligned} \ln(\gamma_X) = & z_X^2 F + \sum m_c (2B_{cX} + ZC_{cX}) \\ & + \sum m_a (2\Phi_{Xa} + \sum m_c \Psi_{cXa}) + \sum \sum m_c m_c' \Psi_{c c' X} \\ & + |z_X| \sum \sum m_c m_a C_{ca} + 2 \sum m_n \lambda_{nX} \\ & + \sum \sum m_n m_c \zeta_{ncX} \end{aligned} \quad (2)$$

$$\ln(\gamma_N) = \sum m_c (2\lambda_{Nc}) + \sum m_a (2\lambda_{Na}) + \sum \sum m_c m_a \zeta_{Nca} \quad (3)$$

where B , C , σ , Ψ , λ and ζ are Pitzer-equation interaction parameters, m_i is the molal concentration, and F and Z are equation functions. In these equations, the Pitzer interaction parameters and the F function are temperature dependent. In these equations, c , a , and n refer to cations, anions, and neutral species, respectively. c' and a' refer to cations and anions, respectively, that differ from c and a . The activity of water (a_w) at 1.01 bar pressure is given by

$$a_w = \exp\left(\frac{-\phi \sum m_i}{55.50844}\right) \quad (4)$$

where ϕ is the osmotic coefficient, which is given by:

$$\begin{aligned}
(\phi - 1) = & \frac{2}{\sum m_i} \left\{ \frac{-A_\phi I^{3/2}}{1 + bI^{1/2}} + \sum \sum m_c m_a (B_{ca}^\phi + ZC_{ca}) \right. \\
& + \sum \sum m_c m_{c'} (\Phi_{cc'}^\phi + \sum m_a \Psi_{cc'a}) \\
& + \sum \sum m_a m_{a'} (\Phi_{aa'}^\phi + \sum m_c \Psi_{ca'a'}) \\
& + \sum \sum m_n m_c \lambda_{nc} + \sum \sum m_n m_a \lambda_{na} \\
& \left. + \sum \sum \sum m_n m_c m_a \lambda_{n,c,a} \right\} \quad (5)
\end{aligned}$$

See Pitzer (1991, 1995) or Marion and Kargel (in press) for a complete description of these equations that govern the temperature dependence of solution thermodynamic properties at 1.01 bar pressure.

In this work, we specified the pressure dependence of equilibrium constants (K), activity coefficients (γ), and the activity of water (a_w) as follows:

The pressure dependence of equilibrium constants was estimated by

$$\ln \left(\frac{K^P}{K^{P^0}} \right) = \left(\frac{-\Delta \bar{V}_r^0 (P - P^0)}{RT} + \frac{\Delta \bar{K}_r^0 (P - P^0)^2}{2RT} \right) \quad (6)$$

where

$$\Delta \bar{V}_r^0 = \sum \bar{V}_i^0 + n \bar{V}_{H_2O}^0 - V_{MX(cr)}^0 \quad (7)$$

$$\Delta \bar{K}_r^0 = \sum \bar{K}_i^0 + n \bar{K}_{H_2O}^0 - K_{MX(cr)}^0 \quad (8)$$

and K^P is the equilibrium constant at pressure P (bars), K^{P^0} is the equilibrium constant at standard pressure P^0 (1.01325 bars), R is the gas constant (83.1451 cm³ bar mol⁻¹ deg⁻¹, Pitzer, 1995), T is temperature (K), \bar{V}_i^0 is the partial molar volume at infinite dilution of the i th constituent, and \bar{K}_i^0 is the molar compressibility at infinite dilution of the i th constituent (Krumgalz et al., 1999). The values of \bar{V}_i^0 and \bar{K}_i^0 used in this paper are compiled in Marion et al. (2005) and Marion and Kargel (in press).

The pressure dependence of ion activity coefficients was estimated with the equation:

$$\ln \left(\frac{\gamma_i^P}{\gamma_i^{P^0}} \right) = \frac{(\bar{V}_i - \bar{V}_i^0)(P - P^0)}{RT} \quad (9)$$

In this equation, the partial molar volume for a cation (M) or anion (X) is given by:

$$\begin{aligned}
\bar{V}_M = & \bar{V}_M^0 + z_M^2 f + 2RT \sum m_a [B_{Ma}^v + (\sum m_c z_c) C_{Ma}^v] \\
& + RT \sum \sum m_c m_a [z_M^2 (B_{ca}^v)' + z_M C_{ca}^v] \quad (10)
\end{aligned}$$

or

$$\begin{aligned}
\bar{V}_X = & \bar{V}_X^0 + z_X^2 f + 2RT \sum m_c [B_{cX}^v + (\sum m_c z_c) C_{cX}^v] \\
& + RT \sum \sum m_c m_a [z_X^2 (B_{ca}^v)' + |z_X| C_{ca}^v] \quad (11)
\end{aligned}$$

The equations for the volumetric Pitzer-equation parameters: f , B^v , B^v , and C^v are compiled in Marion et al. (2005) and Marion and Kargel, in press.

The pressure dependence of the activity of water is calculated by:

$$\ln \left(\frac{a_w^P}{a_w^{P^0}} \right) = \left(\frac{(\bar{V}_w - \bar{V}_w^0)(P - P^0)}{RT} \right) \quad (12)$$

In this equation, the molar volume of water is calculated with

$$\bar{V}_w = \frac{M_w}{1000} \left(\frac{1000 + \sum m_i M_i}{\rho} - \sum m_i \bar{V}_i \right) \quad (13)$$

where M_w and M_i are the molecular masses of water and solution constituents, respectively. The solution density (ρ) in turn is calculated by

$$\rho = \frac{1000 + \sum m_i M_i}{\frac{1000}{\rho^0} + \sum m_i \bar{V}_i^0 + V^{ex}} \quad (14)$$

where m_i is the molal concentration, M_i is the molecular mass, ρ^0 is the density of pure water at a given temperature and pressure, \bar{V}_i^0 is the partial molal volume at infinite dilution, and V^{ex} is the excess volume of mixing given by

$$\frac{V^{ex}}{RT} = f^v + 2 \sum \sum m_c m_a [B_{ca}^v + (\sum m_c z_c) C_{ca}^v] \quad (15)$$

Equations for the Pitzer-equation parameters (f^v , B^v , C^v), \bar{V}_w^0 , \bar{V}_i (Eqs. (12)–(15)) and ρ^0 are compiled in Marion et al. (2005) and Marion and Kargel, in press.

The binary B parameters in Eqs. (1)–(3), (5), (and) (15) are functions of B_{ca}^0 , B_{ca}^1 , and B_{ca}^2 ; similarly, the C parameters in these equations are a function of C^ϕ . The latter parameters are what we will take from the literature or estimate in this paper. In using Fe(III) parameters with the Pitzer equations, we followed the Pitzer version of Christov (2004) that uses an atypical B_{ca}^2 term for all Fe(III) parameters. See Pitzer (1991, 1995) or Marion and Kargel, in press for a complete descriptions of these equations that govern the temperature (Eqs. (1)–(3), (and) (5)) and pressure (Eq. (15)) dependence of solution thermodynamic properties using the Pitzer approach.

The temperature dependence of Pitzer parameters (discussed above) and solubility products (discussed below) are defined by the equation:

$$P = a_1 + a_2 T + a_3 T^2 + a_4 T^3 + a_5 / T \quad (16)$$

where P is the Pitzer parameter or $\ln(K_{sp})$ and T is absolute temperature (K).

2.3. Ferrous/ferric iron solubility products

A thermodynamic approach to estimate the solubility product (K) for a given mineral is as follows:



and

$$\begin{aligned}
K = & (a_{\text{Fe}^{3+}})(a_{\text{Cl}^-})^3 (a_w)^6 \\
= & (\gamma_{\text{Fe}^{3+}})(m_{\text{Fe}^{3+}})(\gamma_{\text{Cl}^-})^3 (m_{\text{Cl}^-})^3 (a_w)^6 \quad (18)
\end{aligned}$$

where a is the activity of the subscripted component, γ is the activity coefficient, and m is the molality (mol kg(H₂O)⁻¹). So given experimental measurements of the molalities (m) and an equilibrium model that can calculate γ and the

activity of water, a_w (Eq. (1)–(5)), one can directly estimate K (Eq. (18)).

Unfortunately, in many cases, especially for insoluble ferric minerals, experimental molalities are lacking, so we need to use an alternative thermodynamic approach to estimate equilibrium constants. K is related to the Gibbs free energy (G) as follows (Nordstrom and Munoz, 1994):

$$\ln(K) = \frac{-\Delta G_r^0}{RT} \quad (19)$$

where ΔG_r^0 is the change in the Gibbs free energies of formation for the components of a given reaction (Eq. (17)):

$$\Delta G_r^0 = \Delta G_{\text{Fe}^{3+}}^0 + 3\Delta G_{\text{Cl}^-}^0 + 6\Delta G_{\text{w}}^0 - \Delta G_{\text{FeCl}_3 \cdot 6\text{H}_2\text{O}}^0 \quad (20)$$

ΔG_r^0 , in turn, can be estimated from enthalpy and entropy data:

$$\Delta G_r^0 = \Delta H_r^0 - T\Delta S_r^0 \quad (21)$$

In what follows, many of the equilibrium constants were estimated based on Eqs. (19) and (21).

Experimental estimates of molalities as a function of temperature allow one to directly estimate the temperature dependence of K , which is how we estimated this temperature dependence whenever such data were available. Where such temperature data were lacking, we used the van't Hoff equation to estimate the temperature dependence:

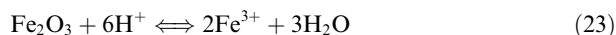
$$\ln(K_{T_2}) = \ln(K_{T_1}) + \frac{\Delta H_r^0}{R} \left[\frac{1}{T_1} - \frac{1}{T_2} \right] \quad (22)$$

In some cases we used both ΔG_r^0 (Eq. (19)) and ΔH_r^0 (Eq. (22)) from the literature to estimate the temperature dependence of solubility products; in some cases we used our experimental estimate of K at a given temperature (K_{T_1}) and ΔH_r^0 from the literature to estimate the temperature dependence with Eq. (22). The accuracy of these extrapola-

tions to lower temperatures is difficult to judge. But Plummer et al. (1988) claim that the temperature range for their PHRQPITZ model is generally 0 to 60 °C, if ΔH_r^0 is known at 298 K and Pitzer (1995) has pointed out that ΔH_r^0 is often nearly constant over a limited temperature range. In all cases, the pressure dependence of equilibrium constants were estimated with Eq. (6).

2.4. FREZCHEM iron model options

There are several reactions (12) that deal with ferric oxide/hydroxide minerals that produce (or consume) H^+ ions. For example, dissolution of ferric iron occurs under strongly acidic conditions:



Conversely, whenever hematite (Fe_2O_3) precipitates, H^+ ions are produced. If we ignore H^+ ion production for these reactions, the aqueous solutions will become charge imbalanced, and as a consequence, the calculated properties of these aqueous solutions will become erroneous. In the modified FREZCHEM model for ferric iron chemistry, we created four options for handling these H^+ ion (pH) calculations.

In Option 1, we ignore pH entirely. This is probably only valid for laboratory experimental data. For example, in Fig. 1, we plotted the model estimated pH and % Fe^{3+} (free) using FeCl_3 inputs and the solution phase ferric hydroxide reactions. Between 0.1 and 2.0 m FeCl_3 , the Fe^{3+} (free) varied from 99.27% to 100.00%; the calculated pH over this FeCl_3 range varied from 3.4 to 2.1 (Fig. 1). At the lowest FeCl_3 concentration of 0.01 m, the predicted Fe^{3+} (free) and pH were 86.65% and 2.95, respectively. Only in dealing with dilute experimental solutions ($\text{Fe}^{3+} < 0.1$ m) is it necessary to explicitly recognize Fe^{3+} -OH complexes.

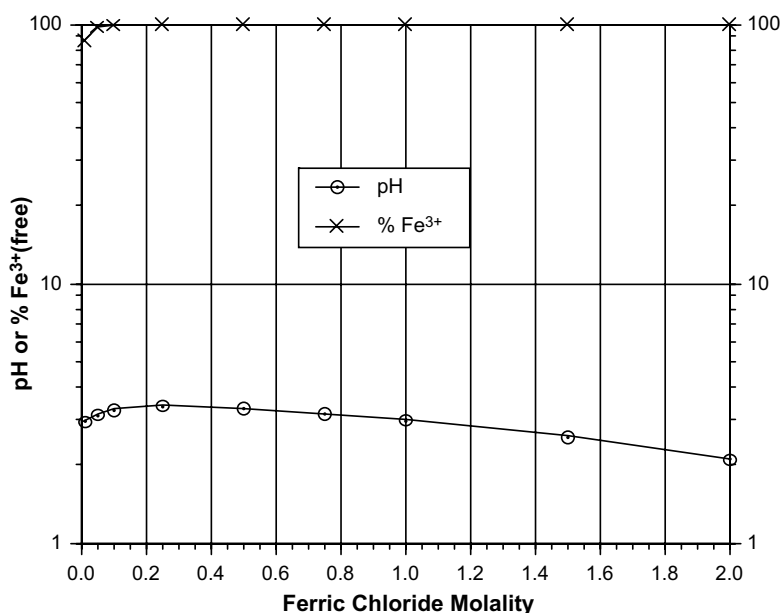


Fig. 1. The distribution of Fe^{3+} (free) and the resulting pH of mixing FeCl_3 salts with water.

In the use of experimental data in this paper (see Sections 3.1 and 3.2), we ignored pH, except in cases where the H⁺ ion was a component of the experimental data.

In Option 2, we fix the pH at a user-designated value (e.g., pH 2.0). In applying the FREZCHEM model to natural environments, it is necessary to recognize explicitly reactions such as Eq. (23). Whenever a reaction such as Eq. (23) takes place, we assume that the H⁺ ions will be neutralized by reaction with minerals releasing cations into the solution. We partitioned the excess H⁺ charge by increasing the aqueous cations proportionally to their existing charges. Allowing the produced H⁺ ions to accumulate as H⁺ ions, instead of other cations, can cause a precipitous drop in pH, which is outside the range of the requested simulation. This scheme helps with the aqueous phase charge balance, and therefore the calculated solution properties such as the activity of water, density, and ionic strength are maintained at reasonable values, which would not be the case if we ignored H⁺ ion production and this led to a serious charge imbalance. However, there is still another source of charge imbalance for Option 2 which is due to the presence of [H⁺] and [HSO₄⁻] because model inputs for this option do not specify the total H input, only the pH. If this charge imbalance is a major concern in acidic systems, Option 3 (described below) provides a better charge balance, but not a fixed pH. In our application of Option 2 to Mars, these charge imbalances averaged 2.7 ± 2.5% (sign ignored, *n* = 24) (range from -10.2% to 5.8%) for the Martian brine evaporation case, and 1.5 ± 1.2% (sign ignored, *n* = 21) (range from -2.1 to 5.8%) for the Martian brine freezing case.

Both Options 3 and 4 have explicit charge balance equations for controlling charge balance and H⁺ ion concentrations and activities. Option 3 is the “acidity” option where acidity is controlled by total H input. In this option, we partitioned ferric oxide/hydroxide produced acidity charge among the solution cations as was done in Option 2. Under the acidic conditions understood to have prevailed across much of Mars for key periods in its hydrogeologic history, the dominant cations are Fe and Mg. Option 4 is the “alkalinity” option where acidity is controlled by alkalinity reactions with solution phase species such as HCO₃⁻ and CO₃²⁻ and solid phases such as calcite (CaCO₃). Whenever a reaction such as Eq. (23) takes place, we assume that the H⁺ ions are neutralized by reactions with carbonate minerals releasing cations into the solution. This is identical to Options 2 and 3, except for the pH range of the dominant cations. Under alkaline conditions, the dominant solution cations are likely to be the abundant alkali and alkaline earth metals, Na, Ca and Mg, except at high pH (>9) where Na and K will likely dominate. At high pH values, Ca and Mg are largely removed from solution through carbonate mineral precipitation.

Redox reactions for Fe³⁺ and Fe²⁺ can be represented by



and

$$E = E^0 - \frac{RT}{nF} \ln \left(\frac{a_{\text{Fe}^{2+}}}{a_{\text{Fe}^{3+}}} \right) \quad (25)$$

The E^0 value is estimated by

$$E^0 = \frac{RT \ln(K)}{nF} = 1.98424 \times 10^{-4} T \log(K) \quad (26)$$

where $\log(K)$ is given by

$$\log(K) = 11.324 + \frac{505.62}{T} \quad (27)$$

which was derived using the van't Hoff equation (Eq. (22)) using $\log(K)$ and ΔH_r^0 data from Nordstrom and Munoz (1994). Another equation that can be used to assess the redox state of an iron system is

$$pE = \log(K) - \log \left(\frac{a_{\text{Fe}^{2+}}}{a_{\text{Fe}^{3+}}} \right) \quad (28)$$

These redox properties (Eqs. (25) and (28)) are outputted whenever Fe²⁺ and Fe³⁺ are system inputs, but these equations are not used to control the behavior of iron systems. Ferric and ferrous iron species are inputted separately and treated as though they are completely independent, which is incorrect, but it can still yield accurate results if separate knowledge provides information on which ferric/ferrous iron phases to use in the modeling and which to exclude. The problem is that kinetics are not a component of the FREZCHEM model, so we cannot deal with control of ferrous and ferric iron as dependent species subject to time-dependent interactions with species such as oxygen gas. For particular types of kinetic issues, where we known in advance that a particular stable phase has difficulty precipitating, we can remove it from the calculations, thus forcing the model to compute the next most thermodynamically favored phase; this can be especially important in some modeling problems with iron oxides/hydroxides and sulfate hydration states.

3. RESULTS

Table 1 includes all the ferrous/ferric minerals that are now part of the FREZCHEM model. Model parameterization for five of the ferrous minerals (footnote “a” in Table 1) were described in a previous publication (Marion et al., 2003) and will not be discussed further in this paper. The new iron chemistries will be presented in three sections representing: iron chlorides, iron sulfates, and iron oxides/hydroxides.

3.1. Iron Chlorides

The Pitzer parameters for Fe(III)-Cl interactions at 298.15 K were taken from Christov (2004). These parameters were extended to lower temperatures by fitting to FeCl₃-Ice data from Linke (1958) (Fig. 2) using the equation:

$$P_T = P_{298.15} + A(298.15 - T) \quad (29)$$

where P is the Pitzer parameter and A is a derived constant. Knowing the freezing point depression of a solution allows one to directly determine the activity of water (a_w) and the solution osmotic coefficient (ϕ , Eq. (4)), which then can serve as the thermodynamic foundation for estimating the

Table 1
Iron minerals and salts currently in the FREZCHEM model

Mineral name	Chemical formula	Molar volume
<i>(A) Ferrous minerals</i>		
	FeCl ₂ ·4H ₂ O ^a	103.01
	FeCl ₂ ·6H ₂ O ^a	133.65
Szomolnokite	FeSO ₄ ·H ₂ O ^a	57.21
Rozenite	FeSO ₄ ·4H ₂ O	99.10 ^b
Melanterite	FeSO ₄ ·7H ₂ O ^a	146.48
	FeSO ₄ ·Na ₂ SO ₄ ·4H ₂ O	162.23 ^c
	FeSO ₄ ·K ₂ SO ₄ ·6H ₂ O	184.01
Siderite	FeCO ₃ ^a	30.49
<i>(B) Ferrous/ferric minerals</i>		
Römerite	Fe(II)Fe(III) ₂ (SO ₄) ₄ ·14H ₂ O	373.96
Bilinite	Fe(II)Fe(III) ₂ (SO ₄) ₄ ·22H ₂ O	507.02
Copiapite	Fe(II)Fe(III) ₄ (SO ₄) ₆ (OH) ₂ ·20H ₂ O	595.21
Voltaite	K ₂ Fe(II) ₃ Fe(III) ₄ (SO ₄) ₁₂ ·18H ₂ O	762.15
<i>(C) Ferric minerals</i>		
Hydromolysite	FeCl ₃ ·6H ₂ O	146.90
	FeCl ₃ ·10H ₂ O	207.59 ^b
Erythrosiderite	FeCl ₃ ·2KCl·H ₂ O	138.84
Mikasaite	Fe ₂ (SO ₄) ₃	129.12
Kornelite	Fe ₂ (SO ₄) ₃ ·7H ₂ O	228.10
Coquimbite	Fe ₂ (SO ₄) ₃ ·9H ₂ O	267.63
Ferricopiapite	Fe ₅ (SO ₄) ₆ O(OH)·20H ₂ O	594.71
	Fe ₂ (SO ₄) ₃ ·2K ₂ SO ₄ ·14H ₂ O	406.95 ^c
Rhombochase	Fe ₂ (SO ₄) ₃ ·H ₂ SO ₄ ·8H ₂ O	295.61
Jarosite	KFe ₃ (SO ₄) ₂ (OH) ₆	162.07
Natrojarosite	NaFe ₃ (SO ₄) ₂ (OH) ₆	156.86
Hydronium jarosite	(H ₃ O)Fe ₃ (SO ₄) ₂ (OH) ₆	178.05
Schwertmannite	FeO(OH) _{0.75} (SO ₄) _{0.125}	24.90
Ferrihydrite	Fe(OH) ₃	28.12
Lepidocrocite	γ-FeO(OH)	22.21
Goethite	α-FeO(OH)	20.76
Hematite	α-Fe ₂ O ₃	30.48

The molar volumes (cm³/mol) are for the solids at 298 K. These molar volumes were derived from (atomic weight/density), except for footnoted entries.

^a See Marion et al. (2003) for the parameterization of these ferrous iron chemistries.

^b Calculated from linear fits to degree of hydration for similar minerals.

^c Calculated using similar minerals as analogues.

value of Pitzer parameters (Eq. (5)). While Eq. (29) was used to estimate the temperature dependence, this equation was converted to our standard format (Eq. (16)) in Table 2.

Parameterization of Fe(III)–Cl interactions to 238.15 K (Fig. 2) allowed us to estimate the solubility products for FeCl₃·6H₂O and FeCl₃·10H₂O (Table 3) based on solubility data (Linke, 1958). The model calculated eutectic for this system occurred at 238.15 K with FeCl₃ = 2.485 m, which is in perfect agreement with a literature value (Linke, 1958). The model-calculated peritectic for FeCl₃·6H₂O–FeCl₃·10H₂O occurred at $T = 272.9$ K with FeCl₃ = 4.60 m, which is in good agreement with $T = 273.4$ K at FeCl₃ = 4.61 m, which was estimated by plotting the two experimental solubilities and then pinpointing the intersection of the two solubility curves.

There is also a scattering of data in Linke (1958) that allowed us to estimate ternary parameters for Fe(III)–Cl interactions with Na, K, or H. There were three datasets at 253, 273, and 298 K for NaCl salt equilibrium with FeCl₃ solutions. Fig. 3A depicts the model fit to the data at 298 K. The calculated peritectic for NaCl–FeCl₃·6H₂O is 0.76 m NaCl and 6.30 m FeCl₃, which are in reasonable agreement with the experimental values of 0.75 m NaCl and 6.08 m FeCl₃. Fig. 3B shows the fit at 273 K. The model describes very well the equilibrium curve for NaCl and the peritectic point where NaCl is in equilibrium with FeCl₃·6H₂O.

There were two data sets (273 and 298 K) on KCl–FeCl₃ mineral equilibrium systems (Linke, 1958). In addition to describing the ternary Fe(III)–K–Cl parameters (Table 2), we also used this data to estimate the solubility product for FeCl₃·2KCl·H₂O (Table 3). Fig. 4A shows the model fit at 298 K. Here the model fit is not nearly as good as was the case for NaCl (Fig. 3). This is also the case at 273 K (Fig. 4B). The dashed line in the latter figure represents an area of the model calculation where the model fails to precipitate FeCl₃·6H₂O. The Christov (2004) paper also showed a problematic fit to this dataset. We will discuss these problematic fits in the section on “Limitations.”

We estimated ternary θ [Fe(III)–H] and Ψ [Fe(III)–H–Cl] parameters (Table 2) based on mineral equilibrium data at 253 and 298 K (Linke, 1958). The fit at 253 K is depicted in Fig. 5. There is a lot of scatter in the experimental data, which unfortunately is a major problem in defining accurate Pitzer equation parameters. In addition to the two mineral equilibrium datasets that we used to define the Fe(III)–H–Cl parameters, there were also five FeCl₃–HCl datasets (248, 253, 258, 263, and 268 K) for equilibria with ice (Linke, 1958). Normally, we would have used such data in model parameterization, but the activities of water (a_w) for pure HCl in these datasets were inconsistent with our previously published acidic model (Marion, 2002). In many cases, older HCl chemistries at subzero temperatures are problematic because it appears that HCl may be present in the ice phase, which affects the equilibrium calculation. See Marion (2002) or Carslaw et al. (1995) for a fuller discussion of this issue. Therefore, we did not use these FeCl₃–HCl–ice data for model parameterization.

3.2. Iron Sulfates

Most of the solubility product parameterizations in Table 3 involve equations of the form:

$$\ln(K) = a_1 + a_5/T \quad (30)$$

The reason for this equation format is because the bulk of the solubility product temperature dependencies were estimated with the van't Hoff equation (Eq. (22)). There were a few notable exceptions that we will first examine, then discuss the more common parameterization approach (Eq. (22) and its derived format, Eq. (30)).

As was the case for Fe(III)–Cl interactions, we also parameterized Pitzer Fe(III)–SO₄ interactions with parameters at 298 K from Christov (2004) that were extended to lower temperatures with freezing point depression data (Fig. 6). However, in marked contrast to the Fe(III)–Cl

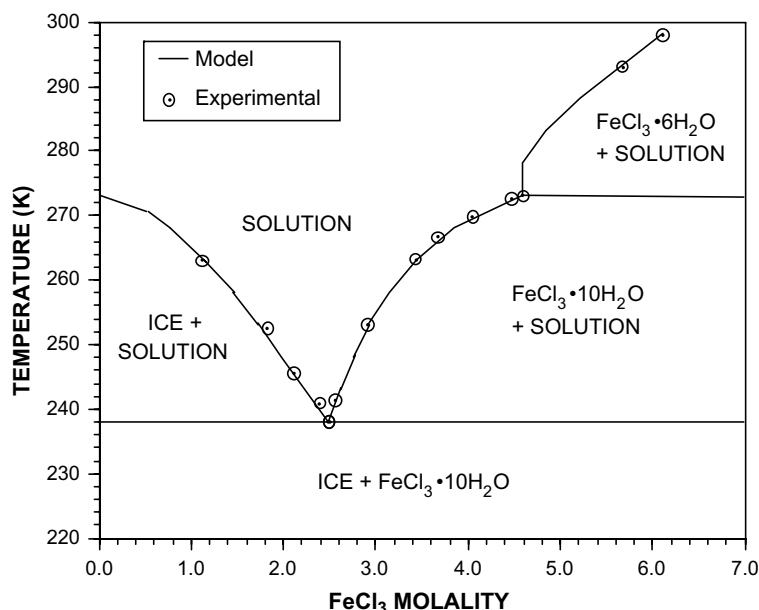


Fig. 2. FeCl_3 equilibria with respect to ice and mineral solid phases as a function of temperature and salt composition.

parameterization (Fig. 2), we relied on $\text{Al}_2(\text{SO}_4)_3$ data as surrogates for $\text{Fe}_2(\text{SO}_4)_3$, both at 298 K (Christov, 2004) and at subzero temperatures (Fig. 6). The resulting binary Fe(III)– SO_4 parameters (Table 2) extended the temperature range down to 263 K. Validation for using $\text{Al}_2(\text{SO}_4)_3$ as surrogates for $\text{Fe}_2(\text{SO}_4)_3$ is discussed in Christov (2004).

How well can these Fe(III)– SO_4 surrogates improve our understanding of ferric sulfate chemistries? There were two datasets from Linke (1958) that apparently included coquimbite (Figs. 7 and 8). In Fig. 8, what we are calling coquimbite is listed as $\text{Fe}_2\text{O}_3 \cdot 3\text{SO}_3 \cdot 9\text{H}_2\text{O}$ in Linke (1958), which is clearly equivalent to $\text{Fe}_2(\text{SO}_4)_3 \cdot 9\text{H}_2\text{O}$ (coquimbite). Fitting a linear equation to the upper nine coquimbite datapoints in this figure extrapolates to $\text{Fe}_2(\text{SO}_4)_3 = 2.103$ m at $\text{H}_2\text{SO}_4 = 0.0$ (Fig. 8). In Fig. 7, a similar extrapolation of a linear equation fitted to the upper six datapoints leads to $\text{Fe}_2(\text{SO}_4)_3 = 2.121$ m at $\text{FeSO}_4 = 0.0$. In Linke (1958), these six datapoints are defined as basic ferric sulfate (B.F.S.) because of their uncertain identity. However, given that both of these extrapolations (Figs. 7 and 8) are nearly identical [2.103 and 2.121 m $\text{Fe}_2(\text{SO}_4)_3$], we assumed that what was called B.F.S. in Fig. 7 is most likely coquimbite.

In Fig. 7, we already know the solubility product of melanterite ($\text{FeSO}_4 \cdot 7\text{H}_2\text{O}$) and the binary Fe(II)– SO_4 parameters from our previous work (Marion et al., 2003). Using this known solubility product as our thermodynamic foundation allowed us to estimate $\Psi_{\text{Fe(II)}, \text{Fe(III)}, \text{SO}_4}$ from this dataset (Table 2). These ternary parameters and the binary Fe(II)– SO_4 and Fe(III)– SO_4 parameters then allowed us to estimate the coquimbite and mikasaite [$\text{Fe}_2(\text{SO}_4)_3$] solubility products at 298 K. The model-calculated mikasaite-melanterite peritectic occurred at $\text{Fe}_2(\text{SO}_4)_3 = 1.73$ m and $\text{FeSO}_4 = 1.035$ m, which are in excellent agreement with the experimental estimate of $\text{Fe}_2(\text{SO}_4)_3 = 1.72$ m and $\text{FeSO}_4 = 1.01$ m.

The kornelite solubility product was estimated by assuming that the ΔG_r^0 of this reaction falls in-between

mikasaite and coquimbite and is entirely due to differences in the ΔG_r^0 of water. That is, $\Delta G_r^0(\text{kornelite}) = \Delta G_r^0(\text{coquimbite}) - 2(-237.7 \text{ kJ mol}^{-1}) = \Delta G_r^0(\text{mikasaite}) + 7(-237.7 \text{ kJ mol}^{-1})$, where $-237.7 \text{ kJ mol}^{-1}$ is $[\Delta G_r^0(\text{coquimbite}) - \Delta G_r^0(\text{mikasaite})]/9$. Note that this calculated value of $-237.7 \text{ kJ mol}^{-1}$ for water is very close to our standard value for water of $-237.1 \text{ kJ mol}^{-1}$ (Table 4). Previous work has shown that this assumption is frequently the case for sulfate minerals (Hemingway et al., 2002).

Fig. 8 depicts coquimbite and rhomboclase equilibria at 298 K as a function of $\text{Fe}_2(\text{SO}_4)_3$ and sulfuric acid. There are many ways of representing the rhomboclase chemical formula [e.g., $\text{HFe(III)(SO}_4)_2 \cdot 4\text{H}_2\text{O}$, $(\text{H}_3\text{O})\text{Fe(III)(SO}_4)_2 \cdot 3\text{H}_2\text{O}$, or $(\text{H}_5\text{O}_2)\text{Fe(III)(SO}_4)_2 \cdot 2\text{H}_2\text{O}$, (Jambor et al., 2000)]. In Linke (1958), rhomboclase is represented as $\text{Fe}_2\text{O}_3 \cdot 4\text{SO}_3 \cdot 9\text{H}_2\text{O}$, which is equivalent to $\text{Fe}_2(\text{SO}_4)_3 \cdot \text{H}_2\text{SO}_4 \cdot 8\text{H}_2\text{O}$, which is how we represent rhomboclase in this paper (Tables 1 and 3). This formulation is equivalent to $2 \times \text{HFe(III)(SO}_4)_2 \cdot 4\text{H}_2\text{O}$.

Given a solubility product for coquimbite as the thermodynamic foundation for model parameter estimation, the coquimbite data in Fig. 8 were used to estimate Fe(III)– HSO_4 binary and ternary parameters (Table 2) that are critical for parameterizing sulfuric acid systems. These binary and ternary Fe(III)– HSO_4 parameters, in turn, were used to estimate the solubility product for rhomboclase at 298 K (Table 3). Our model predicts the peritectic for coquimbite–rhomboclase at 298 K occurs at 0.70 m $\text{Fe}_2(\text{SO}_4)_3$ and 4.51 m H_2SO_4 , which are in good agreement with the literature values of 0.74 m $\text{Fe}_2(\text{SO}_4)_3$ and 4.38 m H_2SO_4 (Linke, 1958) (Fig. 8). The model calculated pH between this peritectic and $\text{H}_2\text{SO}_4 = 8.0$ m ranges from -0.92 to -1.73 . Adjusting these model pH values to the MacInnis convention (Marion, 2002) leads to pH values of -1.8 to -3.25 , respectively, which are in good agreement with field evidence that places rhomboclase precipitation at Eagle

Table 2

Binary, ternary, and volumetric Pitzer-equation parameters derived in this work or taken from the literature (numbers are in computer scientific notation where $e\pm xx$ stands for $10^{\pm xx}$)

	a_1	a_2	a_3	Parameter Temperature range (K)	Parameter source
<i>Pitzer-equation parameter</i>					
$B_{\text{Fe(III),Cl}}^{(0)}$	2.50297e0	-7.2519e-3		238–298	Christov (2004); this work
$B_{\text{Fe(III),Cl}}^{(1)}$	-1.84581e2	6.2455e-1		238–298	Christov (2004); this work
$B_{\text{Fe(III),Cl}}^{(2)}$	1.7199e0			238–298	Christov (2004); this work
$C_{\text{Fe(III),Cl}}^{\phi}$	-3.49365e-1	1.12482e-3		238–298	Christov (2004); this work
$B_{\text{Fe(III),SO}_4}^{(0)}$	1.04326e0	-1.60e-3		263–298	Christov (2004); this work
$B_{\text{Fe(III),SO}_4}^{(1)}$	-4.00430e1	1.751e-1		263–298	Christov (2004); this work
$B_{\text{Fe(III),SO}_4}^{(2)}$	3.07519			263–298	Christov (2004); this work
$C_{\text{Fe(III),SO}_4}^{\phi}$	-5.439e-3	2.00e-5		263–298	Christov (2004); this work
$B_{\text{Fe(III),HSO}_4}^{(0)}$	1.4161e1	-4.96e-2		291–298	This work
$B_{\text{Fe(III),HSO}_4}^{(1)}$	-1.316e2	4.1e-1		291–298	This work
$B_{\text{Fe(III),HSO}_4}^{(2)}$	1.09e1			291–298	This work
$C_{\text{Fe(III),HSO}_4}^{\phi}$	-2.020e0	8.0e-3		291–298	This work
$\Theta_{\text{Fe(II),Fe(III)}}$	-5.0e-2			298	Christov (2004)
$\Psi_{\text{Fe(II),Fe(III),Cl}}$	1.2e-2			298	Christov (2004)
$\Psi_{\text{Fe(II),Fe(III),SO}_4}$	-3.72e-2			298	This work
$\Theta_{\text{Na,Fe(III)}}$	2.183566e1	-1.378504e-1	2.182622e-4	253–298	This work
$\Psi_{\text{Na,Fe(III),Cl}}$	-3.685900e0	2.498632e-2	-4.255333e-5	253–298	This work
$\Psi_{\text{Na,Fe(III),SO}_4}$	-3.0e-2			298	Christov (2004) ^a
$\Theta_{\text{K,Fe(III)}}$	-7.0e-2			298	Christov (2004)
$\Psi_{\text{K,Fe(III),Cl}}$	2.751573e-1	-9.528e-4		273–298	This work
$\Psi_{\text{K,Fe(III),SO}_4}$	-3.0e-2			298	Christov (2004)
$\Theta_{\text{H,Fe(III)}}$	-2.4e-2			253–298	This work
$\Psi_{\text{H,Fe(III),Cl}}$	2.770491e-1	-9.644444e-4		253–298	This work
$\Psi_{\text{H,Fe(III),SO}_4}$	9.0e-3			291–298	This work
$\Psi_{\text{H,Fe(III),HSO}_4}$	0.0			291–298	This work
$\Psi_{\text{SO}_4,\text{HSO}_4,\text{Fe(III)}}$	0.0			291–298	This work
$\Theta_{\text{Mg,Fe(III)}}$	-5.0e-2			298	Christov (2004) ^a
$\Psi_{\text{Mg,Fe(III),Cl}}$	1.2e-2			298	Christov (2004) ^a
$\Psi_{\text{Mg,Fe(III),SO}_4}$	0.0			298	Christov, (2001) ^a
$\Theta_{\text{Ca,Fe(III)}}$	-5.0e-2			298	Christov (2004) ^a
$\Psi_{\text{Ca,Fe(III),Cl}}$	1.2e-2			298	Christov (2004) ^a
$\Psi_{\text{Ca,Fe(III),SO}_4}$	3.0e-2			298	Reardon (1988) ^a
$\lambda_{\text{Fe(III),Gas}}$	3.095e-1			298	Clegg and Brimblecombe (1990) ^b
$\zeta_{\text{Fe(III),Cl,Gas}}$	-1.96e-2			298	Clegg and Brimblecombe (1990) ^b
$\zeta_{\text{Fe(III),SO}_4,\text{Gas}}$	-2.48e-2			298	Clegg and Brimblecombe (1990) ^b
<i>Volumetric parameters</i>					
$B_{\text{Fe(III),Cl}}^{v(0)}$	0.0			273–298	This work
$B_{\text{Fe(III),Cl}}^{v(1)}$	1.07271e-2	-3.40e-5		273–298	This work
$C_{\text{Fe(III),Cl}}^v$	0.0			273–298	This work
$B_{\text{Fe(III),SO}_4}^{v(0)}$	0.0			288–298	This work
$B_{\text{Fe(III),SO}_4}^{v(1)}$	-4.625e-2	1.805063e-4		288–298	This work
$C_{\text{Fe(III),SO}_4}^v$	0.0			288–298	This work
$V_{\text{Fe(III)}}^{(0)}$	-5.70e0	-1.016e-1		273–298	This work
$K_{\text{Fe(III)}}^{(0)}$	1.409230e-1	-1.012854e-3	1.678571e-6	273–298	This work

^a Assumed the same as an analogue from the cited paper.

^b Based on Al-O₂(aq) equilibrium as analogues for Fe(III)-Gas, where soluble gas is O₂(aq), CO₂(aq), or CH₄(aq).

Mt., California in the range from -2.5 to -3.6 (Jambor et al., 2000).

Extension of mikasaite, kornelite, coquimbite, and rhomboclase solubility products to lower temperatures

(Table 3) were all done with Eq. (22) using our calculated equilibrium constants at 298 K and the literature ΔH_r^0 (Table 4). Given a temperature dependence for the rhomboclase solubility product, we used a small rhomboclase

Table 3

Equilibrium constants [as $\ln(K)$] derived in this work or taken from the literature (footnoted)

	a_1	a_2	a_3	a_5	Temperature Range(K)
<i>Solution–solid phase equilibria</i>					
$\text{FeCl}_3 \cdot 6\text{H}_2\text{O} \leftrightarrow \text{Fe}^{3+} + 3\text{Cl}^- + 6\text{H}_2\text{O}$	9.715823e1	-9.428088e-1	2.143448e-3		273–298
$\text{FeCl}_3 \cdot 10\text{H}_2\text{O} \leftrightarrow \text{Fe}^{3+} + 3\text{Cl}^- + 10\text{H}_2\text{O}$	-7.716939e1	2.944561e-1	-7.676424e-5		238–273
$\text{FeCl}_3 \cdot 2\text{KCl} \cdot \text{H}_2\text{O} \leftrightarrow \text{Fe}^{3+} + 2\text{K}^+ + 5\text{Cl}^- + \text{H}_2\text{O}$	-9.315575e1	3.499720e-1			273–298
$\text{FeSO}_4 \cdot 4\text{H}_2\text{O} \leftrightarrow \text{Fe}^{2+} + \text{SO}_4^{2-} + 4\text{H}_2\text{O}$	-6.4360e0	9.68e-3			273–298
$\text{FeSO}_4 \cdot \text{Na}_2\text{SO}_4 \cdot 4\text{H}_2\text{O} \leftrightarrow \text{Fe}^{2+} + 2\text{Na}^+ + 2\text{SO}_4^{2-} + 4\text{H}_2\text{O}$	-6.7220e0				292–298
$\text{FeSO}_4 \cdot \text{K}_2\text{SO}_4 \cdot 6\text{H}_2\text{O} \leftrightarrow \text{Fe}^{2+} + 2\text{K}^+ + 2\text{SO}_4^{2-} + 6\text{H}_2\text{O}$	-3.644195e1	8.970862e-2			273–298
$\text{Fe(II)Fe(III)}_2(\text{SO}_4)_4 \cdot 14\text{H}_2\text{O} \leftrightarrow \text{Fe}^{2+} + 2\text{Fe}^{3+} + 4\text{SO}_4^{2-} + 14\text{H}_2\text{O}$	-6.71649e1			1.19430e4	273–298 ^a
$\text{Fe(II)Fe(III)}_2(\text{SO}_4)_4 \cdot 22\text{H}_2\text{O} \leftrightarrow \text{Fe}^{2+} + 2\text{Fe}^{3+} + 4\text{SO}_4^{2-} + 22\text{H}_2\text{O}$	-3.59423e1			-6.374e2	273–298 ^a
$\text{Fe(II)Fe(III)}_4(\text{SO}_4)_6(\text{OH})_2 \cdot 20\text{H}_2\text{O} + 2\text{H}^+ \leftrightarrow \text{Fe}^{2+} + 4\text{Fe}^{3+} + 6\text{SO}_4^{2-} + 22\text{H}_2\text{O}$	-1.388076e2			2.52691e4	273–298 ^a
$\text{K}_2\text{Fe(II)}_5\text{Fe(III)}_4(\text{SO}_4)_{12} \cdot 18\text{H}_2\text{O} \leftrightarrow 2\text{K}^+ + 5\text{Fe}^{2+} + 4\text{Fe}^{3+} + 12\text{SO}_4^{2-} + 18\text{H}_2\text{O}$	-2.326369e2			4.27325e4	273–298 ^a
$\text{Fe}_2(\text{SO}_4)_3 \leftrightarrow 2\text{Fe}^{3+} + 3\text{SO}_4^{2-}$	-1.010657e2			2.91659e4	273–298 ^a
$\text{Fe}_2(\text{SO}_4)_3 \cdot 7\text{H}_2\text{O} \leftrightarrow 2\text{Fe}^{3+} + 3\text{SO}_4^{2-} + 7\text{H}_2\text{O}$	-5.99039e1			1.63690e4	273–298 ^a
$\text{Fe}_2(\text{SO}_4)_3 \cdot 9\text{H}_2\text{O} \leftrightarrow 2\text{Fe}^{3+} + 3\text{SO}_4^{2-} + 9\text{H}_2\text{O}$	-4.83104e1			1.27729e4	273–298 ^a
$\text{Fe}_5(\text{SO}_4)_6\text{O}(\text{OH}) \cdot 20\text{H}_2\text{O} + 3\text{H}^+ \leftrightarrow 5\text{Fe}^{3+} + 6\text{SO}_4^{2-} + 22\text{H}_2\text{O}$	-1.457056e2			2.71694e4	273–298 ^a
$\text{Fe}_2(\text{SO}_4)_3 \cdot 2\text{K}_2\text{SO}_4 \cdot 14\text{H}_2\text{O} \leftrightarrow 2\text{Fe}^{3+} + 4\text{K}^+ + 5\text{SO}_4^{2-} + 14\text{H}_2\text{O}$	-3.18903e1				273–298 ^a
$\text{Fe}_2(\text{SO}_4)_3 \cdot \text{H}_2\text{SO}_4 \cdot 8\text{H}_2\text{O} \leftrightarrow 2\text{Fe}^{3+} + 2\text{H}^+ + 4\text{SO}_4^{2-} + 8\text{H}_2\text{O}$	-6.56395e1			1.91232e4	273–298 ^a
$\text{KFe}_3(\text{SO}_4)_2(\text{OH})_6 + 6\text{H}^+ \leftrightarrow \text{K}^+ + 3\text{Fe}^{3+} + 2\text{SO}_4^{2-} + 6\text{H}_2\text{O}$	-6.94643e1			1.27007e4	273–298 ^a
$\text{NaFe}_3(\text{SO}_4)_2(\text{OH})_6 + 6\text{H}^+ \leftrightarrow \text{Na}^+ + 3\text{Fe}^{3+} + 2\text{SO}_4^{2-} + 6\text{H}_2\text{O}$	-7.03921e1			1.68380e4	273–298 ^a
$(\text{H}_3\text{O})\text{Fe}_3(\text{SO}_4)_2(\text{OH})_6 + 5\text{H}^+ \leftrightarrow 3\text{Fe}^{3+} + 2\text{SO}_4^{2-} + 7\text{H}_2\text{O}$	-1.056084e2			2.73378e4	273–298 ^a
$\text{FeO}(\text{OH})_{0.75}(\text{SO}_4)_{0.125} + 2.75\text{H}^+ \leftrightarrow \text{Fe}^{3+} + 0.125\text{SO}_4^{2-} + 1.75\text{H}_2\text{O}$	-2.68609e1			8.8054e3	273–298 ^a
$\text{Fe}(\text{OH})_3 + 3\text{H}^+ \leftrightarrow \text{Fe}^{3+} + 3\text{H}_2\text{O}$	-2.44859e1			9.6458e3	273–298 ^a
$\text{FeO}(\text{OH}) + 3\text{H}^+ \leftrightarrow \text{Fe}^{3+} + 2\text{H}_2\text{O}(\text{lepidocrocite})$	-2.47280e1			8.6716e3	273–298 ^a
$\text{FeO}(\text{OH}) + 3\text{H}^+ \leftrightarrow \text{Fe}^{3+} + 2\text{H}_2\text{O}(\text{goethite})$	-2.45667e1			7.4568e3	273–298 ^a
$\text{Fe}_2\text{O}_3 + 6\text{H}^+ \leftrightarrow 2\text{Fe}^{3+} + 3\text{H}_2\text{O}$	-5.27235e1			1.57556e4	273–298 ^a
<i>Solution phase equilibria</i>					
$\text{Fe}^{2+} + \text{H}_2\text{O} \leftrightarrow \text{FeOH}^+ + \text{H}^+$	3.93e-1			-6.6390e3	273–298 ^b
$\text{Fe}^{2+} + 2\text{H}_2\text{O} \leftrightarrow \text{Fe}(\text{OH})_2 + 2\text{H}^+$	8.53e-1			-1.43965e4	273–298 ^b
$\text{Fe}^{2+} + 3\text{H}_2\text{O} \leftrightarrow \text{Fe}(\text{OH})_3^- + 3\text{H}^+$	-2.0238e1			-1.52480e4	273–298 ^b
$\text{Fe}^{3+} + \text{H}_2\text{O} \leftrightarrow \text{FeOH}^{2+} + \text{H}^+$	1.2205e1			-5.2318e3	273–298 ^b
$\text{Fe}^{3+} + 2\text{H}_2\text{O} \leftrightarrow \text{Fe}(\text{OH})_2^+ + 2\text{H}^+$	1.5827e1			-8.6115e3	273–298 ^b
$\text{Fe}^{3+} + 3\text{H}_2\text{O} \leftrightarrow \text{Fe}(\text{OH})_3 + 3\text{H}^+$	1.2940e1			-1.25083e4	273–298 ^b
$\text{Fe}^{3+} + 4\text{H}_2\text{O} \leftrightarrow \text{Fe}(\text{OH})_4^- + 4\text{H}^+$	3.915e0			-1.59961e4	273–298 ^b

(Numbers are in computer scientific notation, where $e \pm xx$ stands for $10^{\pm xx}$).^a Derived using Eqs. (19) and (22) with ΔG_r^0 and ΔH_r^0 from the text and Table 4.^b Derived using Eqs. (19) and (22) with ΔG_r^0 and ΔH_r^0 from Nordstrom and Munoz (1994).

dataset at 291 K ($n = 4$) (Linke, 1958) to develop a temperature dependence for the Fe(III)–HSO₄ binary parameters (Table 2) using the Eq. (29) approach.

There were experimental data for three other iron sulfates that we added to our model, namely: FeSO₄·Na₂SO₄·4H₂O, FeSO₄·K₂SO₄·6H₂O, and Fe₂(SO₄)₃·K₂SO₄·14H₂O. There were six datapoints for FeSO₄·Na₂SO₄·4H₂O between 292 and 298 K (Linke, 1958). There was no significant temperature dependence over this narrow temperature range, so we assigned a constant equilibrium constant to

this chemistry (Table 3). There were six datapoints for FeSO₄·K₂SO₄·6H₂O solubility over the temperature range from 273 to 298 K (Linke, 1958) (Fig. 9). A linear equation (Table 3) gave a reasonably good fit to this equilibria (Fig. 9). There were 18 datapoints for the Fe₂(SO₄)₃·K₂SO₄·14H₂O system at 298 K that allowed us to estimate the solubility product for Fe₂(SO₄)₃·K₂SO₄·14H₂O (Fig. 10). This a relatively poor fit at least in part because of the experimental variability. For example, the five highest experimental K₂SO₄ concentrations (0.77 to 0.93 m)

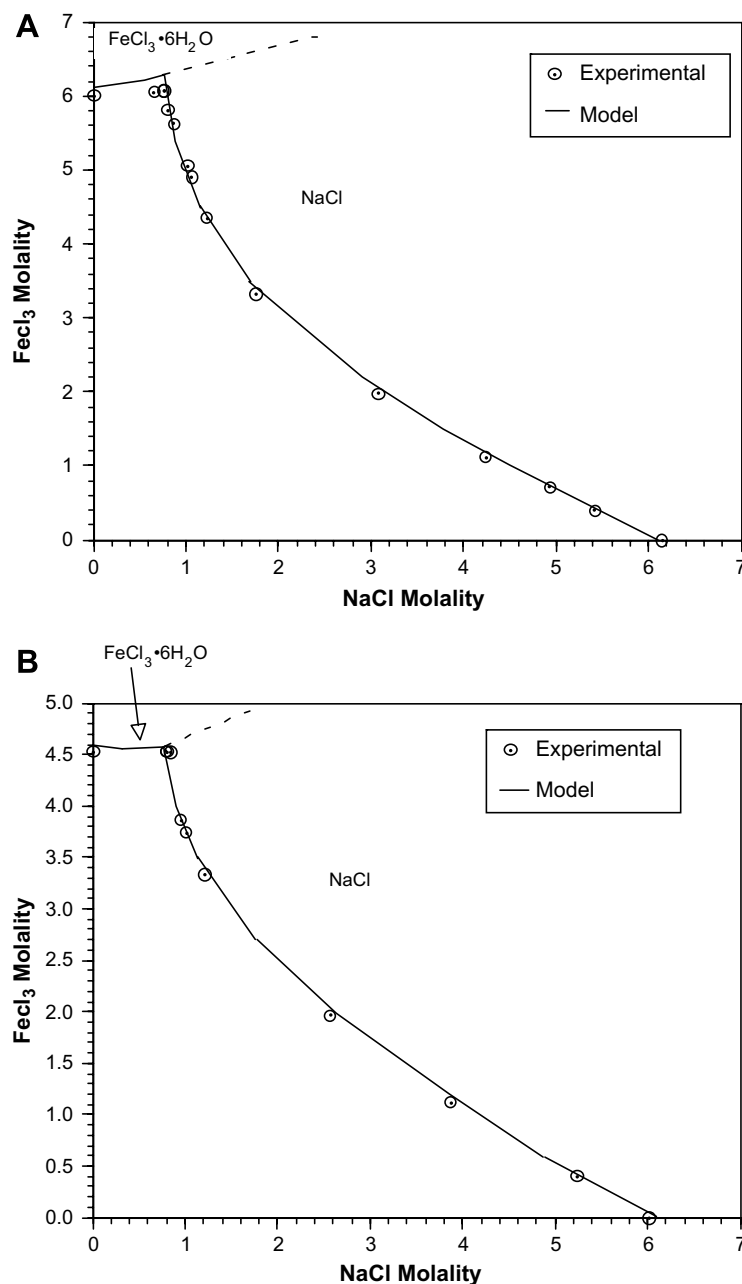


Fig. 3. The solubility of FeCl₃ and NaCl salts at (A) 25 °C and (B) 0 °C.

represent the K₂SO₄-Fe₂(SO₄)₃-K₂SO₄·14H₂O peritectic, which ideally should have a fixed composition. Such variability, as well as other factors, makes it difficult to accurately parameterize such chemistries. The shape of our model fit (Fig. 10) is very similar to the fit of Christov (2004) (his Fig. 9) for this dataset.

The rozenite solubility product was estimated by assuming that the ΔG_r^0 of this reaction falls in-between melanterite and szomolnokite and is entirely due to differences in the ΔG_r^0 of water (Hemingway et al., 2002). That is, $\Delta G_r^0(\text{rozenite}) = \Delta G_r^0(\text{melanterite}) - 3(-238.4\text{kJ mol}^{-1}) = \Delta G_r^0(\text{szomolnokite}) + 3(-238.4\text{kJ mol}^{-1})$. This is identical to the technique used to estimate the kornelite solubility product (see previous discussion).

All other ferrous/ferric iron sulfate solubility products in Table 3 not explicitly discussed above based directly, or indirectly, on experimental data were estimated with Eqs. (19), (20), and (22) based on published Gibbs free energy and enthalpy data (Table 4).

3.3. Iron oxides/hydroxides

In contrast to the previously discussed parameterization of iron chlorides and sulfates that were based, in part, on experimental solubility measurements, all the iron oxide/hydroxide solubility products were based on application of Eq. (22) using the ΔG_r^0 and ΔH_r^0 data of Table 4. See Eqs. (19) and (20) for how these reaction constants were

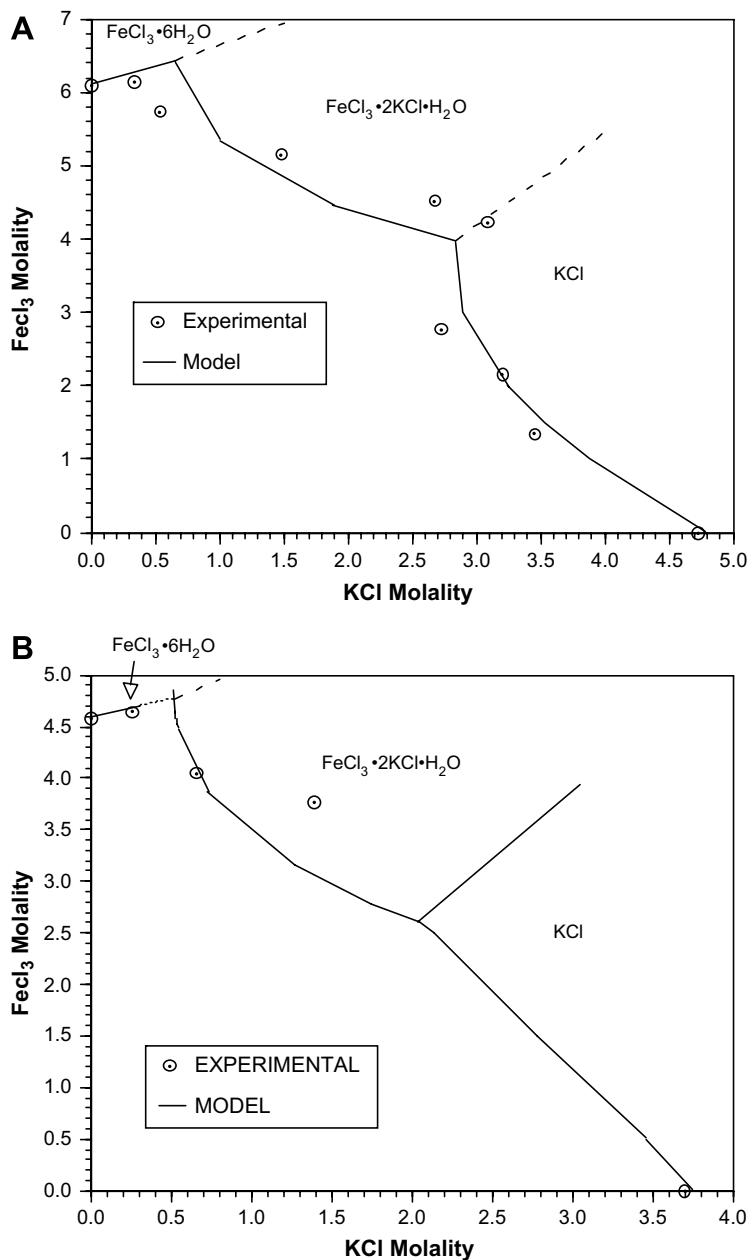


Fig. 4. The solubility of FeCl₃ and KCl salts at (A) 25 °C and (B) 0 °C.

calculated. In a few cases, we had to adjust the experimental ΔH_f^0 data based on non-ideal formulas to represent our ideal formulas (Tables 1 and 3). For example, the ΔG_f^0 values for schwertmannite were given for two non-ideal compositions with waters of hydration as well as for the ideal schwertmannite formula with no waters of hydration (Fig. 11) (Majzlan et al., 2004). We assumed a linear relation for ΔH_f^0 , as was the case for ΔG_f^0 , to estimate a $\Delta H_f^0 = -590.5 \text{ kJ mol}^{-1}$ (Fig. 11 and Table 4) for an ideal schwertmannite formula (Table 1).

Another notable difference between iron oxides/hydroxides and iron chlorides/sulfates are the marked differences in solution concentrations. For example, the ionic strength of pure FeCl₃·6H₂O at 298 K (Fig. 2) is 36.6 m; similarly,

the ionic strength of pure Fe₂(SO₄)₃·9H₂O (coquimbite) at 298 K is 31.5 m (Figs. 7 and 8). Such high concentrations for our FREZCHEM model are problematic and will be discussed in the section on “Limitations.” In marked contrast, the Fe(III) solubilities of jarosite [KFe₃(SO₄)₂(OH)₆] and hematite (Fe₂O₃) at pH 2.0 are approximately 0.0004 and 0.000055 m. In fact, it is the low solubilities of these iron oxides/hydroxides and their slow approach to equilibrium that necessitated an alternative approach (Eqs. (19), (20), and (22)) for estimating solubility products. This marked contrast in iron mineral solubilities is also problematic for application of the FREZCHEM model, which will be discussed further in the sections on “Limitations” and “Mars Applications”.

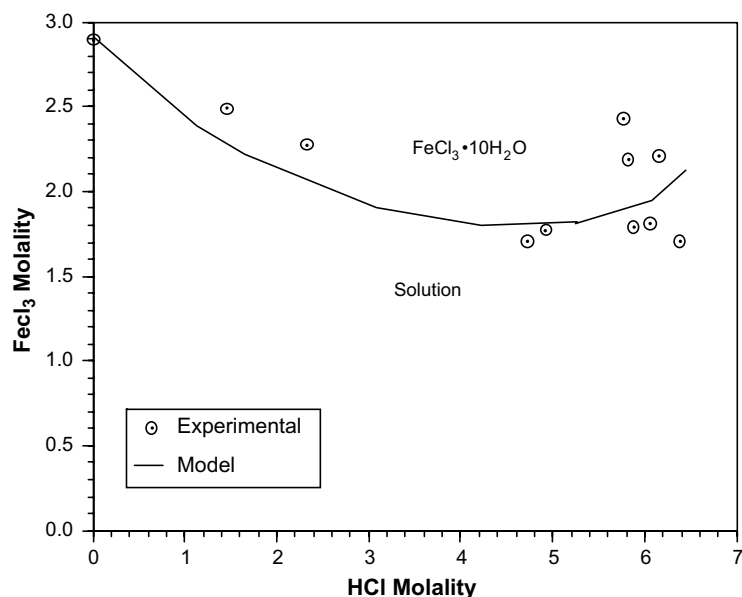


Fig. 5. The solubility of $\text{FeCl}_3 \cdot 10\text{H}_2\text{O}$ as a function of HCl at -20°C .

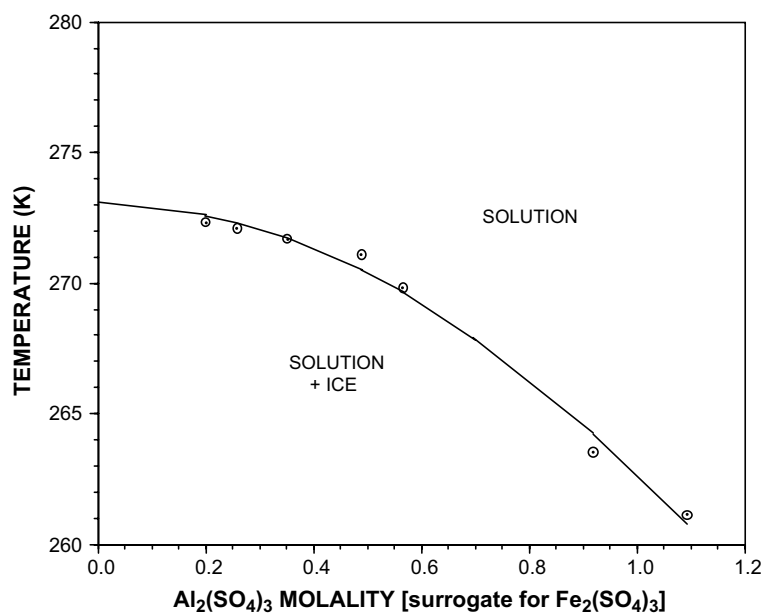


Fig. 6. The "ice" line of $\text{Al}_2(\text{SO}_4)_3$ as a surrogate for $\text{Fe}_2(\text{SO}_4)_3$.

Also included in Table 3 are the Fe(II) and Fe(III) solution complexes with the hydroxide ion (OH^-). All of the ΔG_f^0 and ΔH_f^0 data for these reactions were taken from Nordstrom and Munoz (1994). These solution-phase equilibria play a significant role in the distribution of soluble Fe(II) and Fe(III) (Fig. 12) and, as a consequence, in the calculation of mineral equilibria. Below pH 3.0, virtually all the ferric (and ferrous) iron is present as Fe^{3+} (and Fe^{2+}); above pH 3.0, iron chemistry equilibria necessitates an explicit recognition of hydroxyl complexes (Fig. 12).

3.4. Density and pressure parameterization

The FREZCHEM model is structured to predict density and the effects of pressure on chemical equilibria (Eqs. (6)–(15)). Implementation of these equations requires a specification of the partial molar volume (V_i^0) and compressibility (K_i^0) of individual species (e.g., Fe^{3+}) and binary Pitzer equation volumetric parameters (e.g., B_{ca}^v).

There were two density datasets for mixtures of FeCl_3 - NaCl at 273 and 298 K (Linke, 1958). At each temperature, there were seven datapoints. These two datasets were used

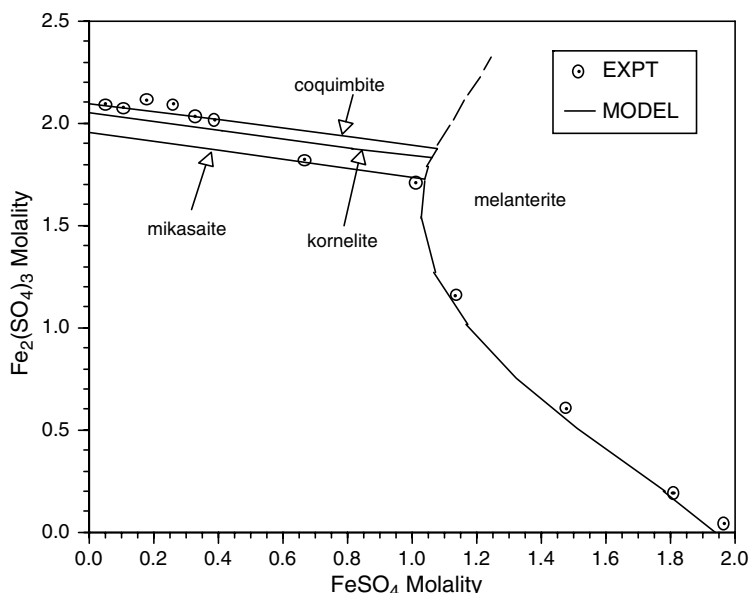


Fig. 7. Equilibria among melanterite, mikasaite, kornelite, and coquimbite as a function of ferric sulfate and ferrous sulfate concentrations at 25 °C.

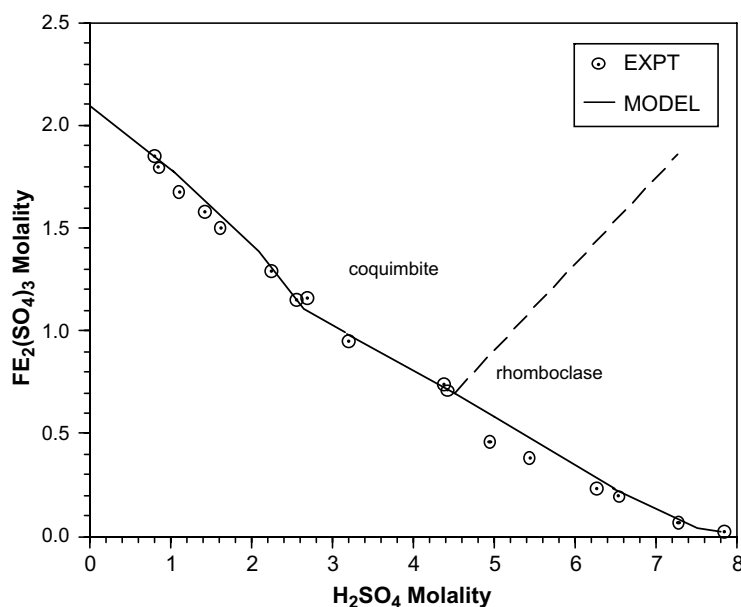


Fig. 8. Equilibria between coquimbite and rhomboclase as a function of ferric sulfate and sulfuric acid concentrations at 25 °C.

to estimate the temperature dependence of $(B_{\text{Fe}^{3+},\text{Cl}}^{(1)V})$ and $(\bar{V}_{\text{Fe}^{3+}}^0)$ (Table 2). In these calculations, we assigned $(B_{\text{Fe}^{3+},\text{Cl}}^{(0)V})$ and $(C_{\text{Fe}^{3+},\text{Cl}}^V)$ values of 0.0. Allowing the latter parameters to vary did not improve the prediction of density. At 298 K, the standard error (SE) in predicting densities between 1.196 and 1.460 g cm⁻³ was 0.24%; at 273 K, the SE in predicting densities between 1.218 and 1.423 g cm⁻³ was 0.79%.

Application of the model to predict the pressure dependence of equilibrium constants (Eqs. (6)–(8)) requires an estimate of the compressibility of the Fe³⁺ ion. Assigning

the Fe³⁺ ion a surrogate value of $-85.28 \text{ cm}^3 \text{ mol}^{-1} \text{ bar}^{-1}$ (the La³⁺ ion, Millero, 2001) led to a poor fit to the density data. Instead, we made the assumption that a linear fit to K⁺ and Ca²⁺ compressibility data over the 273–298 K temperature range (Millero, 2001) would extrapolate reasonably well for Fe³⁺. The resultant temperature-dependent compressibility equation for the Fe³⁺ ion is given in Table 2. Our estimates of the molar volume and compressibility for Fe³⁺ at 298 K were $-35.99 \text{ cm}^3 \text{ mol}^{-1}$ and $-11.85 \times 10^{-3} \text{ cm}^3 \text{ mol}^{-1} \text{ bar}^{-1}$, which are similar in magnitude to PO₄³⁻ values of $-30.46 \text{ cm}^3 \text{ mol}^{-1}$ and $-16.71 \times 10^{-3} \text{ cm}^3 \text{ mol}^{-1} \text{ bar}^{-1}$ (Millero, 2001).

Table 4

The ΔG and ΔH of formation for the solution phase species and the solid phases used to estimate the equilibrium constants and their temperature dependence (see Eqs. (19), (20), and (22))

Species	ΔG_f^0 (kJ mol ⁻¹)	ΔH_f^0 (kJ mol ⁻¹)	Reference
<i>Solution phases</i>			
H ⁺	0.0	0.0	Robie and Hemingway (1995)
Na ⁺	-261.5	-240.3	Robie and Hemingway (1995)
K ⁺	-282.5	-252.1	Robie and Hemingway (1995)
Fe ²⁺	-90.0	-91.1	Robie and Hemingway (1995)
Fe ³⁺	-16.7	-49.9	Robie and Hemingway (1995)
Al ³⁺	-489.4	-538.4	Robie and Hemingway (1995)
OH ⁻	-157.3	-230.0	Robie and Hemingway (1995)
SO ₄ ²⁻	-744.0	-909.3	Robie and Hemingway (1995)
H ₂ O	-237.1	-285.8	Robie and Hemingway (1995)
<i>Solid phases</i>			
Fe(II)Fe(III) ₂ (SO ₄) ₄ ·14H ₂ O	-6486	-7730	Hemingway et al. (2002)
Fe(II)Fe(III) ₂ (SO ₄) ₄ ·22H ₂ O	-8410	-10,121	Hemingway et al. (2002)
Fe(II)Fe(III) ₄ (SO ₄) ₆ (OH) ₂ ·20H ₂ O	-9971	-11,824	Hemingway et al. (2002)
K ₂ Fe(II) ₅ Fe(III) ₄ (SO ₄) ₁₂ ·18H ₂ O	-14,499	-16,860	Hemingway et al. (2002)
Fe ₂ (SO ₄) ₃	—	-2585.2	Majzlan et al. (2005)
Fe ₂ (SO ₄) ₃ ·7H ₂ O	—	-4692.2	Hemingway et al. (2002)
Fe ₂ (SO ₄) ₃ ·9H ₂ O	—	-5293.7 ^a	Majzlan et al. (2006)
Fe ₃ (SO ₄) ₆ O(OH)·20H ₂ O	-9899	-11,767	Hemingway et al. (2002)
Fe ₂ (SO ₄) ₃ H ₂ SO ₄ ·8H ₂ O	—	-5864.4 ^a	Majzlan et al. (2006)
KFe ₃ (SO ₄) ₂ (OH) ₆	-3309.8	-3829.6	Drouet and Navrotsky (2003)
NaFe ₃ (SO ₄) ₂ (OH) ₆	-3256.7	-3783.4	Drouet and Navrotsky (2003)
(H ₃ O)Fe ₃ (SO ₄) ₂ (OH) ₆	-3232.3	-3741.6	Drouet and Navrotsky (2003)
FeO(OH) _{0.75} (SO ₄) _{0.125}	-518.0	-590.5 ^{a,b}	Majzlan et al. (2004)
Fe(OH) ₃	-708.5	-827.1	Majzlan et al. (2004)
γ-FeO(OH)	-480.1	-549.4	Majzlan et al. (2003)
α-FeO(OH)	-489.8	-559.5	Majzlan et al. (2003)
α-Fe ₂ O ₃	-744.4	-826.2	Robie and Hemingway (1995)

^a Adjusted from the non-ideal formula of the original paper to represent the ideal formula in column 1.

^b See Fig. 11.

We examined four datasets that included the density of Fe₂(SO₄)₃ solutions. One of these density datasets was from Linke (1958). The three remaining datasets were at 288.15,

290.65, and 291.15 K (ICT, 1928). The 290.65 K dataset was classified as discordant with respect to the 288.15 and 291.15 K datasets (ICT, 1928); so we discarded the

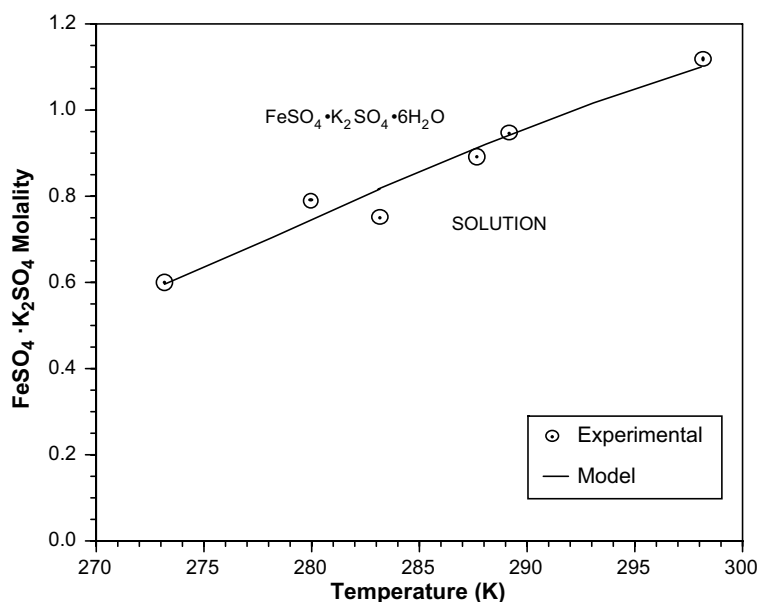


Fig. 9. The solubility of FeSO₄·K₂SO₄·6H₂O as a function of composition and temperature.

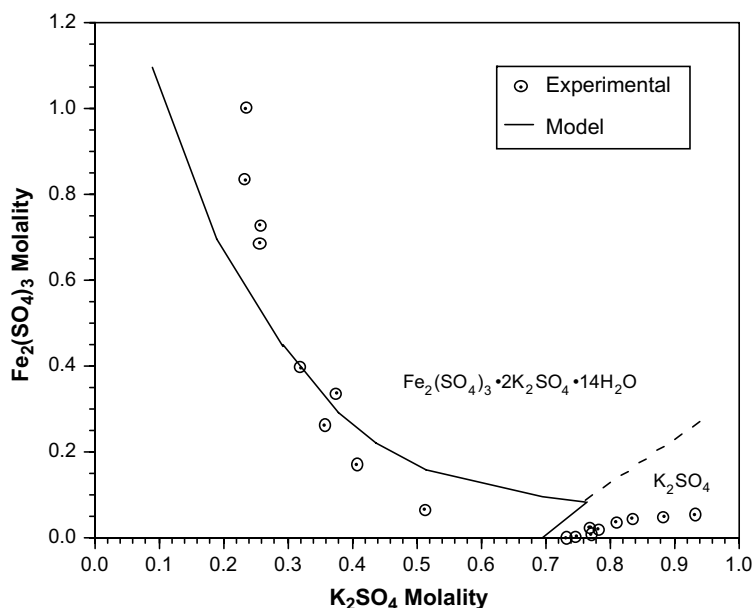


Fig. 10. Equilibria between K_2SO_4 and $\text{Fe}_2(\text{SO}_4)_3 \cdot 2\text{K}_2\text{SO}_4 \cdot 14\text{H}_2\text{O}$ as a function of $\text{Fe}_2(\text{SO}_4)_3$ and K_2SO_4 concentrations at 25 °C.

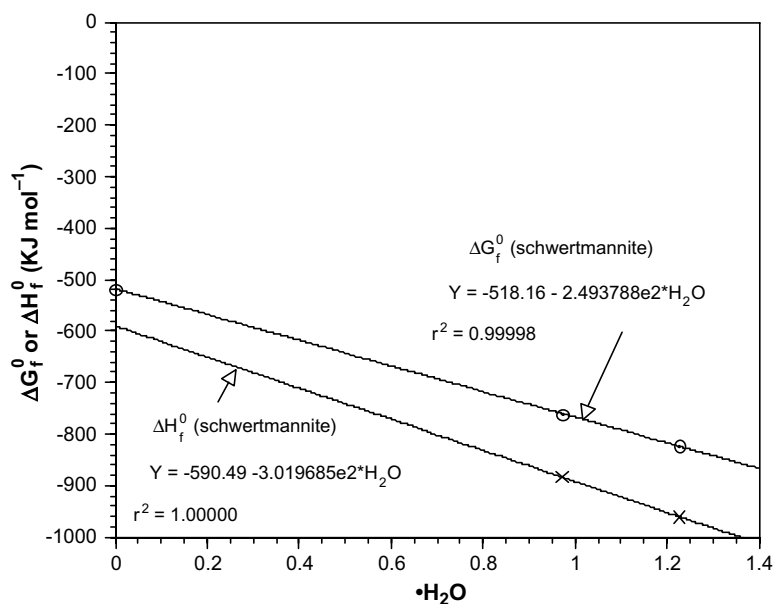


Fig. 11. The ΔG_f^0 and ΔH_f^0 for schwertmannite as a function of associated waters of hydration.

290.65 K dataset. We only included data on $\text{Fe}_2(\text{SO}_4)_3$ concentrations ≤ 1 m because of discrepancies among the datasets at higher concentrations. The temperature-dependent volumetric parameters for $\text{Fe}^{3+}\text{-SO}_4^{2-}$ are given in Table 2. The SE of the model in estimating the densities of the three datasets ($n = 28$) was 0.24%. The SE of the individual datasets varied from 0.06% to 0.14%. This was a less than optimal overall fit because of minor, but important, discrepancies among the datasets. All of these datasets date back to 1935 or earlier (ICT, 1928; Linke, 1958). Hopefully improved experimental datasets in the future will help us better define the densities of Fe(III)-SO_4 solutions.

4. VALIDATION

The paucity of ferric iron data and problems related to frequent metastable appearance and persistence of phases makes it difficult to validate the model. While model fits to experimental data are encouraging and point out the self consistency of the model and data inputs (Figs. 2–5, 7–10), they are not validation, which requires comparison to independent data for multicomponent solutions. The only previously cited example where we compared the model to independent data was our comparison of pH values where rhomboclase precipitates (see Section 3.2). Our model pre-

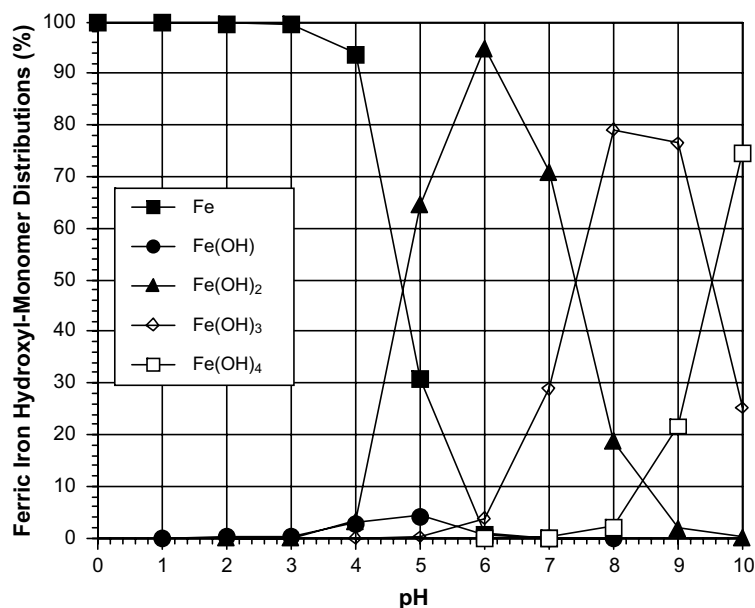


Fig. 12. The distribution of Fe^{3+} (free) and hydroxyl complexes as a function of pH.

dicts that rhomboclase should precipitate at pH values lower than -1.8 (Fig. 8), which is in good agreement with rhomboclase precipitation at Eagle Mt., California in the range from -2.5 to -3.6 (Jambor et al., 2000).

Comparing model predictions of mineral stabilities in acidic systems can be used to at least qualitatively validate the model. For example, the Rio Tinto region of southern Spain contains highly acidic waters often dominated by ferric-sulfate chemistries. Melanterite, rozenite, rhomboclase, szomolnokite, copiapite, coquimbite, hexahydrite, halotrichite, and gypsum have been found precipitating in the Rio Tinto (Buckby et al., 2003). Only halotrichite $[\text{Fe(III)Al}_2(\text{SO}_4)_4 \cdot 22\text{H}_2\text{O}]$ is not currently in the FREZCHEM model. An aqueous Rio Tinto example is given in Table 5. Because of limitations of the FREZCHEM model, we had to lump Al with Fe and Cu + Zn + Mn with Ca in order to get a reasonable estimate of the charge balance. This approximation surely introduces some significant error for this simulation, but currently we have no acceptable

alternative. Nevertheless, as we show below, the model seems to make accurate predictions of mineral stability.

On the molar scale the charge imbalance was -0.0930 equivalents l^{-1} , which we assumed was due to H^+ . This H^+ ion concentration led to model pH values of 1.86–2.21 in our simulations, which falls within the pH range for Rio Tinto waters (1.08–2.86, Fernandez-Remolar et al., 2005); this could be fortuitous, but we suggest that despite simplifications and approximations, the model is generating reasonably accurate output. Converting experimental mg l^{-1} to mol l^{-1} is simple; converting molarity (mol l^{-1}) to molality [$\text{mol kg}(\text{H}_2\text{O})^{-1}$] requires a special algorithm (Marion, 2007) for estimating the density of this solution, which in this case worked out to be 1.0731 g cm^{-3} at 294 K (room temperature). Molality is the required format for input into the FREZCHEM model and virtually all other chemical thermodynamic models for concentrated brines. While we lumped constituents for estimating the charge balance, we only used the actual Fe(III) and Ca concentrations (see values in parentheses in Table 5) in our simulations.

If we run the chemical composition of Table 5 through the FREZCHEM model at 298 K, the model predicts that hematite and hydronium jarosite should precipitate (Table 6). If we remove hematite, the most stable ferric oxide, from the mineral database, the model then predicts that goethite and hydronium jarosite should precipitate (Table 6). We ran these simulations removing one constituent at a time until nothing further precipitated. The first five constituents removed in these simulations were various ferric oxide/hydroxide minerals. The last constituent removed was ferricopiapite. After removing ferricopiapite, the only remaining ferric minerals that might be potentially precipitable were mikasaite, kornelite, and coquimbite (Fig. 7). However, the approximate $\text{Fe}_2(\text{SO}_4)_3$ concentration for this solution was only about

Table 5
The elemental composition of the Rio Tinto region, Angeles Spring water sample (Fernandez-Remolar et al., 2004)

Elements	Concentration (mg/l)	Molarity (mol/l)	Molality (mol/kg(H ₂ O))
Fe (+Al)	18,800	0.4094	0.3976 [Fe(III) = 0.2609] ^a
Mg	1,200	0.0494	0.0480
Ca (+Cu + Zn + Mn)	437	0.0073	0.0071 (Ca = 0.0009) ^b
H	—	0.0930 ^c	0.0904
S	23,000	0.7173	0.6967

^a This is the Fe(III) concentration used in the simulations.

^b This is the Ca concentration used in the simulations.

^c The H^+ concentration was determined by charge imbalance.

Table 6

Model estimates of the stability of various ferric minerals in the Rio Tinto region, Angeles Spring water (Fernandez-Remolar et al., 2004, 2005)

Minerals removed from database	Minerals in precipitates
No minerals removed (see Table 1)	Hematite, hydronium jarosite
-Hematite	Goethite, hydronium jarosite
-Hematite,-goethite	schwertmannite, hydronium jarosite
-Hematite,-goethite, -schwertmannite	Lepidocrocite, hydronium jarosite
-Hematite,-goethite, -schwertmannite, lepidocrocite	Ferrihydrite, hydronium jarosite
-Hematite,-goethite, -schwertmannite, -lepidocrocite, -ferrihydrite	Hydronium jarosite
-Hematite,-goethite, -schwertmannite, -lepidocrocite, -ferrihydrite, -hydronium jarosite	Ferricopiapite
-Hematite,-goethite, -schwertmannite, -lepidocrocite, -ferrihydrite, -hydronium jarosite, -ferricopiapite	Nothing

0.2 m, which is considerably undersaturated with respect to these three minerals (Fig. 7).

How do these model calculations compare to the minerals actually found precipitating in the Rio Tinto region? For the Angeles Spring case, the iron minerals that are precipitating are goethite and hydronium jarosite (Fernandez-Remolar et al., 2005), which is what our model predicts in the absence of hematite (Table 6). This makes sense because goethite usually forms as a kinetically unstable precursor to hematite. The three dominant iron oxide/hydroxide minerals precipitating in the Rio Tinto waters are hematite, goethite, and schwertmannite (Fernandez-Remolar et al., 2005), which is in good agreement with our model that predicts that these are the three most stable ferric oxide/hydroxide minerals in these acidic ferric-sulfate waters (Table 6).

The waters running through these systems are clearly supersaturated with respect to these stable ferric oxide/hydroxide minerals. If true chemical thermodynamic equilibria existed in these systems, the ferric iron concentrations would be a small fraction of the field-measured concentrations. For example, equilibrium with respect to jarosite would have a Fe(III) concentration of 0.0004 m at pH 2.0 (see Section 3.3), rather than 0.2609 m (Table 5). The Rio Tinto system, however, is extremely spatially heterogeneous (mineralogically and in elemental composition, pH, and temperature) and temporally dynamic (Fernandez-Remolar et al., in press); this situation is expected to produce marked metastability, so it is both surprising and reassuring that we were able to make accurate mineralogical simulations.

Despite the approximations and large uncertainties of some inputs, the equilibrium FREZCHEM model as newly parameterized for ferric iron chemistries should be a useful tool for studying the precipitation, paragenesis, and diagenesis of iron minerals, which we will examine next in “Mars Applications.”

5. MARS APPLICATIONS

We developed simulations for evaporation and freezing of a hypothetical Martian fluid based on a composition resulting from acid weathering of basalt (with olivine) at pH 1.9 (see Figs. 5 and 6 in Tosca et al. (2005)). The initial composition of this solution was: Na = 3.16e–4 m, K = 1.05e–4 m, Ca = 2.85e–3 m, Mg = 5.58e–2 m, Fe(II) = 2.79e–2 m, Fe(III) = 2.79e–2 m, Cl = 4.20e–3 m, and

SO₄ = 0.1265 m. In this compositional derivation, we assumed that total Fe = Mg, and Fe(II) = Fe(III); the latter assumption is purely arbitrary, but it allows for pure and mixed ferrous/ferric minerals. We also made minor adjustments of the major constituents (Fe, Mg, SO₄) to assure a perfect charge balance for our initial composition. In these simulations, precipitated salts were not allowed to re-equilibrate with the solution phase (fractional crystallization) as solutions evaporated or froze.

5.1. Primary salt precipitation

A classic approach to evaporite mineral precipitation and brine evolution in closed basins on Earth (Hardie and Eugster, 1970) has been adapted to explore chemical divides, divergent brine evolution, and salt assemblages possible on Mars (Tosca and McLennan, 2006). The divides appear as a result of primary rock compositions, weathering processes, the initial stoichiometry of major cations and anions, and liquid lines-of-descent controlled by precipitation of major stable and metastable phases. Whereas that approach is generally applicable to any system undergoing evaporitic precipitation, and it is readily adapted to freeze-driven brine evolution as well, the specific architecture of chemical divides depends heavily on conditions, including temperature, which for Mars certainly would include subzero conditions where ice is a major precipitating phase and many salts precipitate in highly hydrated forms. In the chemical divide architecture under development by Tosca and McLennan (2006), the database and calculations are limited currently to 25 °C. The new addition to FREZCHEM of ferrous and ferric iron chemistry at low temperatures—approximate though it may be—allows a more realistic consideration of chemical divides on Mars as well as in terrestrial evaporitic and freezing brine systems.

We have not yet applied our model in a systematic way so as to establish low-temperature chemical divides and a full classification of Martian brine types and salt assemblages in iron-rich systems. We have made some test applications. We used the FREZCHEM model to simulate the consequences of evaporating and freezing of a hypothetical iron-rich Martian brine. Because it is unlikely that ferric oxide/hydroxide minerals are primary precipitates, we removed the latter minerals from our simulations. The idea behind these simulations was to examine the consequences of evaporation and freezing on the environments for even-

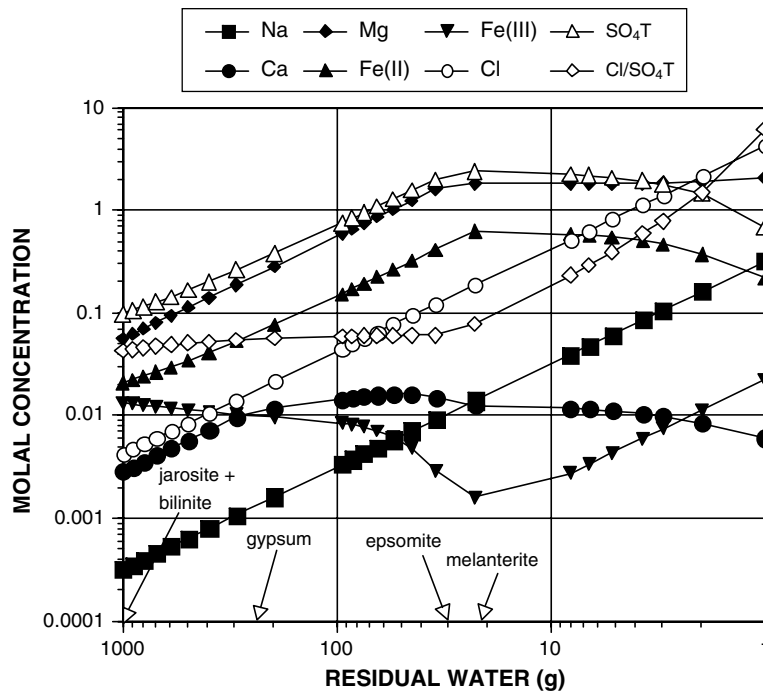


Fig. 13. The molal concentrations of a hypothetical Martian brine during evaporation at 0 °C. Arrows indicate where solid phases start to precipitate.

tual diagenesis of iron minerals due to alternating dry/wet and freeze/thaw cycles.

Fig. 13 depicts the change in ion concentrations as our hypothetical Martian brine evaporated at 273 K with pH 2.0. The initial solution was supersaturated with jarosite

and bilinite. Later as evaporation proceeded, first gypsum, then epsomite, and finally melanterite began precipitating (Fig. 13). What began as a predominantly Fe–Mg–SO₄ solution, ended up as a predominantly Mg–Cl solution. In these simulations, *K* was reduced from 10⁻⁴ to 10⁻⁸ m

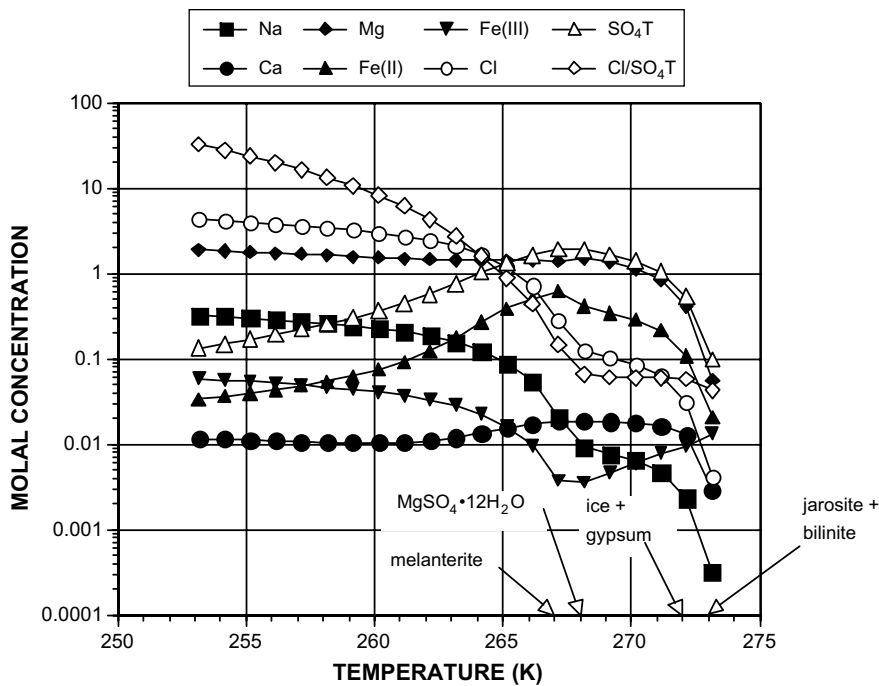


Fig. 14. The molal concentrations of a hypothetical Martian brine during freezing between 0 and -20 °C. Arrows indicate where solid phases start to precipitate.

initially due to jarosite formation. Due to this low concentration, we did not include *K* in Fig. 13 (and Fig. 14) since that would have stretched the *Y* axis thus obscuring the details of other elements at higher molalities. Running this simulation at pH 1.0 led to the same suite of minerals, except that jarosite did not precipitate at this low pH. We also ran this fractional crystallization at pH 3.0, which led to a broader range of precipitates including: gypsum, epsomite, melanterite, mirabilite, $\text{MgSO}_4 \cdot 12\text{H}_2\text{O}$, jarosite, and natrojarosite.

We ran this Martian brine through a freezing process down to 253 K (Fig. 14). At 273 K with pH 2.0, the starting solution was supersaturated with jarosite and bilinite. At 272 K, ice and gypsum began forming. The ice formation process led to a rapid increase in most of the solution constituents (Fig. 14). Eventually $\text{MgSO}_4 \cdot 12\text{H}_2\text{O}$ and melanterite were predicted to precipitate.

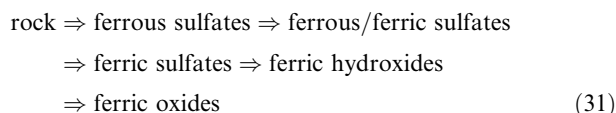
Virtually the same minerals precipitated during evaporation at 273 K and freezing to 253 K (cf., Figs. 13 and 14). Only epsomite ($\text{MgSO}_4 \cdot 7\text{H}_2\text{O}$) during evaporation and $\text{MgSO}_4 \cdot 12\text{H}_2\text{O}$ during freezing were different. That jarosite and bilinite precipitated at the initiation of both processes is clearly understandable because these two cases had exactly the same composition in the same environment ($T = 273 \text{ K}$, $P = 1.01 \text{ bars}$, pH 2.0). The much more rapid concentration of salts during freezing is due to ice formation in a relatively dilute initial solution. Evaporation of our initial solution before freezing would have led to a slower compositional change. The last datapoint in the evaporation simulation contained 1.0 g H_2O ; for the freezing process, the last datapoint also contained 1.0 g H_2O . So the evaporation and freezing processes reduced the solutions to the same water level. But one striking difference between these two processes is what happened to $\text{SO}_{4\text{T}}$ ($=\text{SO}_4 + \text{HSO}_4$) and Cl. At the end of the evaporation process, the Cl/ $\text{SO}_{4\text{T}}$ ratio was 6.2 (Fig. 13); for the freezing process, the final Cl/ $\text{SO}_{4\text{T}}$ ratio was 32.6 (Fig. 14). So despite the similarities in the types of sulfate salts precipitated, the freezing process at lower temperatures was much more effective than evaporation at higher temperatures in precipitating SO_4 from solution and increasing the residual Cl/ $\text{SO}_{4\text{T}}$ ratio.

Table 7
Paragenetic sequences of Fe-sulfate minerals from pyrite oxidation (adapted from Jambor et al., 2000)

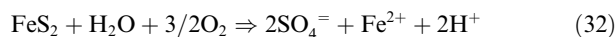
Time	Chile	Laboratory	Iron Mt., California	
Early	Pyrite	Pyrite	Pyrite	
		Melanterite	Melanterite	
		Siderotil		
		Rozenite	Rozenite	
		Szomolnokite	Szomolnokite	Szomolnokite
		Römerite	Rhombochase	Copiapite
		Quenstedtite		Römerite
		Coquimbite	Coquimbite	Coquimbite
		Pickeringite	Römerite	Kornelite
		Copiapite		Rhombochase
Late	Jarosite	Voltaite	Voltaite	
			Halotrichite–bilinite	

5.2. Paragenesis

Data strongly suggest that iron minerals on Mars have likely gone through paragenesis (mineral transformations over time) (Herkenhoff et al., 2004; Kargel, 2004a,b; Squyres et al., 2004, 2006; McLennan et al., 2005; Jolliff and McLennan, 2006). In Table 7 are examples of iron transformations from pyrite to jarosite on Earth. Overall, paragenesis of iron minerals on Earth, when subjected to oxidizing aqueous conditions, follows the weathering sequence (Jambor et al., 2000):



The first weathering step is due to hydrolysis of silicates and oxidation of sulfides. The latter is probably more important in most of the types of environments where ferrous sulfate and ferrous chloride solutions are generated. Iron sulfide oxidation may be represented by the following generic reaction:



On Earth, aqueous mineral precipitation and especially reduction–oxidation chemistry of sulfur and iron is commonly microbially mediated (Douglas, 2005). The ubiquity of life in many aqueous environments makes it difficult to know exactly what reactions would not occur on geological timescales in the absence of the catalytic properties of life, and which are merely slightly spurred by metabolizing agents. Sulfide and iron oxide chemistry, including reaction 32 and most steps in the generalized reaction 31 sequence, are especially tied inextricably to life in many places on Earth, as exemplified by the Rio Tinto deposits and their underground habitats (Fernandez-Remolar et al., in press). Other means of generating acidic iron sulfate solutions, common in volcanic crater lakes and in Yellowstone hydrothermal pools, include venting of SO_2 into water, oxidation to sulfuric acid, and attack on ferrous iron silicates (Kargel et al., 1999); this mechanism also has key and perhaps essential involvement of life for the conditions on Earth. It is a different question whether such chemistry would also occur without biological activity, perhaps requiring only a bit more time or slightly more thermodynamically and kinetically favorable physical conditions. Simple laboratory experiments generally indicate that, indeed, life is not necessary for these processes to occur, if time, the degree of supersaturation, or temperature are allowed to compensate for what life catalyzes on Earth.

In Table 7, the first iron sulfate minerals to precipitate are ferrous sulfates which follow a clearcut decreasing hydration pattern from melanterite ($\text{FeSO}_4 \cdot 7\text{H}_2\text{O}$) to rozenite ($\text{FeSO}_4 \cdot 4\text{H}_2\text{O}$) to szomolnokite ($\text{FeSO}_4 \cdot \text{H}_2\text{O}$). This pattern occurs because dehydration is likely caused by kinetic factors, ionic strength, evaporation, or freezing induced concentration of salts and lowering of water activity. Such dehydration could be responsible for the prevalence on Mars of the mineral kieserite ($\text{MgSO}_4 \cdot \text{H}_2\text{O}$), instead of higher hydrates of magnesium sulfate (Gendrin et al.,

Table 8
The paragenesis of a hypothetical Martian brine at 298 K, 1 bar pressure, and pH 2.0

Time	Fe oxides/ hydroxides	Jarosites	Fe(III)SO ₄	Fe(II)SO ₄	Mixed Fe(III)– Fe(II)SO ₄	MgSO ₄	CaSO ₄	Concentration factor	Ionic strength (m)
(early)									
1			Coquimbite					57.2	31.5
2			Kornelite					54.7	30.1
3			Mikasaite					50.0	27.4
4						Kieserite		46.1	25.4
5				Szomolnokite				43.3	23.8
6	Ferrihydrite			Rozenite				39.8	21.9
7						Hexahydrite		36.0	19.8
8						Epsomite		32.3	17.7
9				Melanterite				31.8	17.5
10					Voltaite			16.4	8.98
11					Römerite			14.9	8.14
12							Anhydrite	8.26	4.44
13							Gypsum	3.85	2.05
14 (late)					Bilinite			1.00	0.39
		Na-jarosite			Copiapite			1.00	0.38
			Ferricopiapite					1.00	0.38
	Schwertmannite							1.00	0.41
	Lepidocrocite	H ₃ O- jarosite/ K-jarosite						1.00	0.41
	Goethite							1.00	0.40
	Hematite							1.00	0.40

2005; Marion and Kargel, 2005; Marion et al., 2006c). Over time, if an oxidizing environment prevails, these ferrous sulfate minerals are transformed into mixed ferrous/ferric sulfates, then into ferric sulfates, followed by ferric hydroxides, and finally ferric oxides (Eq. (31)).

Using the FREZCHEM model with the full suite of iron minerals and salts (Table 1) and the above Martian composition at 298 K and pH 2.0 resulted in the precipitation of hematite, which is in excellent agreement with the Meridiani Planum findings (Clark et al., 2005; Tosca et al., 2005). However, it is unlikely that nearly insoluble ferric oxide/hydroxide minerals are primary precipitates based on paragenetic processes on Earth (Schwertmann et al., 1999; Jambor et al., 2000; Table 7) or our understanding of hematite formation on Mars (Christensen et al., 2001; Herkenhoff et al., 2004; Klingelhöfer et al., 2004; Squyres et al., 2004, 2006; Jolliff and McLennan, 2006). Therefore, we reran the simulation after removing hematite from the mineral database (Table 1). The next most insoluble iron mineral that precipitated was goethite. Removing goethite led to the simultaneous precipitation of lepidocrocite, hydronium jarosite, and jarosite (Table 8), which we and many other researchers think are some likely primary mineral phases and may be involved also in a complex paragenetic sequence, including diagenesis (e.g., McLennan et al., 2005). The initial composition (see above) was supersaturated with ten minerals (Table 8). After these ten minerals were removed from the mineral database (Table 1), it was necessary to evaporate the solution before any other mineral in our entire database (81 solid phases) could precipi-

tate. The first of these evaporite minerals was gypsum; the last mineral in our database to precipitate was coquimbite (Table 8). Precipitation of coquimbite involved a 57.2× concentration of the initial solution to an ionic strength of 31.5 m before coquimbite could precipitate (Table 8).

Paragenesis of iron minerals typically evolves from highly soluble minerals early in mineral deposition to less soluble minerals later in mineral formation (Table 7). These patterns (Table 7) are similar but clearly not identical to those of our simulation (Table 8). Specific mineral deposition depends ultimately on initial compositions and environmental constraints. There is no way that our hypothetical composition (see above) at pH 2.0 could, for example, ever lead to rhomboclase precipitation because the latter mineral requires pH values <−1.8 (MacInnis convention) (Fig. 8). So these simulations provide clues but not definitive answers to Martian paragenesis.

On Mars today, there is abundant evidence for iron minerals such as hematite, goethite, and jarosites (Christensen et al., 2001, 2004; Bandfield, 2002; Bishop et al., 2004; Klingelhöfer et al., 2004; Morris et al., 2004, 2006; Squyres et al., 2004, 2006; Clark et al., 2005; Golden et al., 2005; Navrotsky et al., 2005; Tosca et al., 2005; McSween, 2006; Ming et al., 2006). If one is looking for other secondary iron minerals on Mars, strong candidates include lepidocrocite, schwertmannite, ferricopiapite, copiapite, and bilinite (Table 8). There is spectroscopic support for, but not proof of, hydrous iron sulfate minerals such as ferricopiapite, szomolnokite, and/or rozenite on Mars (Lane et al., 2004). The specific iron minerals on Mars provide clues to the geochemical and

climatic histories of Mars. For example, the presence of jarosite on Mars clearly indicates a highly acidic environment. Such “keystone” minerals are powerful constraints on speculations concerning the hydrogeochemical, climatic, and possible biological histories of remote planets and moons. Simulations such as Table 8 provide clues to minerals that are or might be present on Mars.

5.3. Diagenesis

Cycling of dry/wet and freeze/thaw environments could have played important roles in diagenetic processes on Mars (Crowley et al., 2006). In both evaporation and freezing, the final solutions are dominated by Mg–Cl, which is substantially different from the initial Fe–Mg–SO₄ dominated systems. The last salts to precipitate under these two processes would be MgCl₂ and NaCl salts. Also as these evaporite deposits are rewetted or the frozen deposits rewarmed, the first soluble salts that would be released are MgCl₂ and NaCl. Dissolution of MgCl₂ and NaCl salts has been suggested as a possible cause for vug formation in Meridiani Planum sedimentary rocks and for the downward movement of Cl through layered deposits in Endurance Crater (Squyres et al., 2004, 2006; Clark et al., 2005; Tosca et al., 2005). For example, Clark et al. (2005) suggested that temperature increases from below the salt eutectic (≈ 238 K) to above the eutectic would preferentially release Cl salts, which could lead to stratigraphic deposits. Our freezing-point depression simulation clearly favors the release of Cl salts, at least up to 265 K (Fig. 14). Our estimate of the eutectic for this Martian brine was based on a simplification of the chemical composition of the residual solution at 253.15 K (Fig. 14). We removed minor constituents (Fe(II), Fe(III), Ca, H, SO_{4T}) and ran the simulation with the remaining major constituents (Na, Mg, Cl) that were charge balanced. The actual eutectic occurred at 237.95 K (-35.2 °C) with MgCl₂·12H₂O starting to precipitate at 239.15 K (-34.0 °C) and NaCl·2H₂O (hydrohalite) at the eutectic.

With respect to vugs, Peterson and Wang (2006) have suggested that these plate-shaped voids in the Meridiani Planum formed from the melting of MgSO₄·11H₂O, which is the same salt that we have designated as MgSO₄·12H₂O. Uncertainty exists with respect to waters of hydration associated with this MgSO₄ salt (see Peterson and Wang, 2006). This salt melts into epsomite and water above about 2 °C. Based on the difference of our model simulations between freezing (Fig. 14) and evaporation (Fig. 13), this highly hydrated magnesium sulfate would indicate that the Meridiani sulfates formed initially from freezing rather than evaporation. Low-temperature brine chemistry may have profound implications for the geochemical and geological history of Mars and affect our interpretation of the planet's paleoclimatic history. For example, incongruent melting of massive deposits of MgSO₄·12H₂O, CaSO₄·2H₂O and other hydrates could result in formation of subsurface brines and help explain outflow channels, gullies, chaotic terrain, sink holes, and other fluvial and collapse landforms; remobilized salts and brines may generate salt diapirs, saline mud volcanoes, cross-cutting salt veins, and other salty bodies pro-

duced by brine reactivation (Kargel, 2004a; Montgomery and Gillespie, 2005; Peterson and Wang, 2006; Rodriguez et al., 2006; Kargel et al., in press).

Another diagenetic process on Mars is the formation of hematite concretions (Herkenhoff et al., 2004; Klingelhöfer et al., 2004; Squyres et al., 2004, 2006; Jolliff and McLennan, 2006). In both of our simulations, Fe(II) concentrations approached 1.0 m (Figs. 13 and 14). Also, melanterite (FeSO₄·7H₂O) is the dominant ferrous salt that precipitated. Initial salt depositions likely would have included relatively soluble salts such as melanterite (Table 8). Over time as these soluble salts were slowly oxidized, they could easily have lead to the formation of insoluble ferric oxide/hydroxide minerals, such as hematite and goethite, both of which are prevalent on Mars (Christensen et al., 2001, 2004; Bandfield, 2002; Morris et al., 2004, 2006; Squyres et al., 2004, 2006; Ming et al., 2006; Klingelhöfer et al., 2004; McSween, 2006) and Earth (Table 6).

Our simulations show that FREZCHEM includes the foundations for precipitation of soluble iron minerals due to either evaporation (Fig. 13) or freezing (Fig. 14). Both modes of precipitation of primary iron minerals could serve as the iron source for the eventual precipitation of relatively insoluble ferric minerals. Which of these two cycles and the relative contribution of each for primary phase precipitation and subsequent diagenetic processes on Mars is still very much an open question. Also unsettled is the role of dehydration/hydration cycles involving solid hydratable salts and vapor phases but lacking a liquid phase, as should occur under conditions of exceeding low relative humidity (Feldman et al., 2004). The diagenetic effects of these processes, as on Earth, may substantially affect the extant mineral assemblages and affect our ability to interpret primary depositional environments and infer paleoclimates.

6. MODEL LIMITATIONS AND CONCLUSIONS

The paucity of ferric iron data is a severe limitation for accurately parameterizing ferric iron chemistry. There are only limited Cl and SO₄ databases across limited temperature and pressure ranges. Precipitation of ferric Cl and SO₄ salts are not always rapid, which means that equilibration times can often be for periods up to a year (Linke, 1958). One of the difficulties inherent in working with ferric iron is that (except in very acid or reducing conditions) this iron rapidly reacts with oxygen leading ultimately to precipitation of ferric oxide/hydroxide minerals. So the experimental precipitates can be mixed ferric salts that are often difficult to identify (see Linke (1958) for examples). For Fe₂(SO₄)₃ Pitzer parameterizations, we had to use Al₂(SO₄)₃ parameters as surrogates. The fit of these Al₂(SO₄)₃ parameters to Fe₂(SO₄)₃ data led to reasonable estimates of Fe₂(SO₄)₃ solubilities (Figs. 7 and 8). So this use of a surrogate may not be a severe limitation.

The paucity of experimental data is clearly reflected in the limited temperature ranges for many Pitzer parameters (Table 2) and equilibrium constants (Table 3). In some cases, these parameters are only defined at 298 K. Applications of the FREZCHEM model using these parameters assume a constant value across all temperatures. Applications

of temperature-dependent equations (Tables 2 and 3) to temperatures lower than their database temperatures (listed in Tables 2 and 3) are based on simple mathematical extrapolation of these equations, which is often necessary for many reactions at subzero temperatures (Marion, 2001, 2002; Marion et al., 2003, 2006a).

In some cases, the experimental data appear to be poor. For example, there is a lot of scatter of experimental $\text{FeCl}_3\text{-HCl}$ data (Fig. 5) and $\text{Fe}_2(\text{SO}_4)_3\text{-K}_2\text{SO}_4$ data (Fig. 10). Pitzer model parameterization is critically dependent on the accuracy of the experimental data. Poor datasets or base parameters will lead to poor parameterizations, a factor discussed in recent papers that made pleas for new experimental data (Christov, 2004; Majzlan et al., 2006; Tosca et al., 2007).

A factor that likely contributes significantly to inaccuracies are the unusually high ionic strengths of soluble FeCl_3 and $\text{Fe}_2(\text{SO}_4)_3$ salts. For example, at 298 K, the ionic strength of a saturated FeCl_3 solution is 36.6 m (Fig. 2). The ionic strength of coquimbite at 2.1 m and 298 K is 31.5 (Fig. 7). Most previous work in developing the FREZCHEM model largely focused on ionic strengths ≤ 20 m. An example where high ionic strengths likely were a factor in model breakdown is Fig. 4B. The dashed line in the upper left corner of this figure is where the activity coefficient model collapsed and suddenly $\text{FeCl}_3\cdot 6\text{H}_2\text{O}$ was no longer precipitable. Another example where salt behavior seems odd is in Fig. 2, between 273 and 278 K, where the concentration of $\text{FeCl}_3\cdot 6\text{H}_2\text{O}$ is basically constant. It was difficult with the FREZCHEM model to even establish the peritectic point between $\text{FeCl}_3\cdot 6\text{H}_2\text{O}$ and $\text{FeCl}_3\cdot 10\text{H}_2\text{O}$. In dilute solutions, as salt concentrations increase, the ionic strength increases, and activity coefficients decrease up to a point, beyond which they increase. In extremely high concentrations, various activity coefficients may be increasing and decreasing simultaneously and rapidly, which can lead to difficulties in modeling this behavior. In an earlier paper dealing with strong acid chemistries (Marion, 2002), we also noted similar behavior where datapoints in the stability field of $\text{K}_5\text{H}_3(\text{SO}_4)_4$ were becoming vertically asymptotic, which led to a rapid decline in activity coefficients, a phenomenon that was not always predicted well by the model.

Another problem in applying the FREZCHEM model has to do with the state of chemical equilibria for ferric iron solutions and minerals. The actual aqueous concentrations for the Rio Tinto case (Tables 5 and 6) fall somewhere between the solubility of ferricopiapite and mikasaite. The only observed precipitates identified in this particular case were goethite and hydronium jarosite, which agrees with our model simulation without hematite (Table 6). But the actual field solutions (Table 5) are highly supersaturated with goethite and hydronium jarosite, as well as with a series of other minerals (Table 6). The degree of supersaturation observed is far in excess of what is common for many other sulfates, such as magnesium sulfate hydrates (Hogenboom et al., 1995); but the general experience is that sulfate solutions are slow to reach equilibrium. The metastability of iron oxides is well known, and so it also appears that ferric iron sulfates are similar.

To simulate the full spectrum of iron chemistries for a specific site necessitates running "paragenetic" simulations that cover the entire range of solution concentrations and mineral precipitates from highly soluble salts such as mikasaite and coquimbite to insoluble salts such as hematite and goethite. One cannot assume, as was done in previous applications of the FREZCHEM model, that the solution and mineral phases are simultaneously in thermodynamic equilibrium. The new version of FREZCHEM still lacks a capability to incorporate kinetics into the calculations.

As Mars exploration and our understanding of Mars improves, it is likely that two key underpinnings of Mars brine and salt chemistry models will involve epochal and short-term dynamic shifts and perhaps oscillations in local and global conditions of solution pH and atmospheric oxygen (Crowley et al., 2006). Such changes are already apparent in existing data and interpretations of Mars (Bibring et al., 2006; Wang et al., 2006), as they are for Earth. The temporal and geographic controls on these parameters, in addition to the long-discussed shifts and oscillations in global temperatures, remain poorly constrained. At least now there is a geochemical thermodynamic model, FREZCHEM, that can be used as an aid in modeling and understanding these complexities of Martian history and rock deposits, and also may be used further as a tool for astrobiological exploration using remote sensing data and *in situ* geological methods (Crowley et al., 2007).

ACKNOWLEDGMENTS

Funding was provided by a NASA Planetary Geology and Geophysics Project, "An Aqueous Geochemical Model for Cold Planets," a NASA EPSCoR Project, "Building Expertise and Collaborative Infrastructure for Successful Astrobiology Research, Technology, and Education in Nevada," and a NASA IES Project, "Remote Spectral Characterization of Terrestrial Life Forming Environments for Planetary Exploration." We thank Lisa Wable for assistance in preparing the manuscript. We also thank Nicholas Tosca, Christomir Christov, and Joel Hurowitz for constructive comments that improved our paper.

REFERENCES

- Bandfield J. L. (2002) Global mineral distributions on Mars. *J. Geophys. Res.* **107**(E6). doi:10.1029/2001JE001510.
- Bibring J.-P., Langevin Y., Gendrin A., Gondet B., Poulet F., Berthe M., Soufflot A., Arvidson R., Mangold N., Mustard J., Drossart P. and the Omega Team (2005) Mars surface diversity as revealed by the OMEGA/Mars Express observations. *Science* **307**, 1576–1581.
- Bibring J.-P., Langevin Y., Mustard J.F., Poulet F., Arvidson R., Gendrin A., Gondet B., Mangold N., Pinet P., Forget F. and the OMEGA team. (2006) Global mineralogical and aqueous Mars history derived from OMEGA/Mars Express data. *Science* **312**, 400–404.
- Bishop J. L., Darby Dyar M., Lane M. D. and Banfield J. F. (2004) Spectral identification of hydrated sulfates on Mars and comparison with acidic environments on Earth. *Inter. J. Astrobiol.* **3**, 275–285.
- Buckby T., Black S., Coleman M. L. and Hodson M. E. (2003) Fe-sulphate-rich evaporative mineral precipitates from the Rio Tinto, southwest Spain. *Mineral. Mag.* **67**, 263–278.

- Burns R. G. (1987) Ferric sulfates on Mars. *J. Geophys. Res.* **92**, E570–E574.
- Carslaw K. S., Clegg S. L. and Brimblecombe P. (1995) A thermodynamic model of the system HCl-HNO₃-H₂SO₄-H₂O, including solubilities of HBr, from <200 to 328 K. *J. Phys. Chem.* **99**, 11,557–11,574.
- Catling D. C. (1999) A chemical model for evaporites on early Mars: possible sedimentary tracers of the early climate and implications for exploration, *J. Geophys. Res.* **104**, 16,453–16,470.
- Catling D. C., Wood S. E., Leovy C., Montgomery D. R., Greenberg H., Glein C. R. and Moore J. M. (2006) Light-toned layered deposits in Juventae Chasma, Mars. *Icarus* **181**, 26–51.
- Christensen P. R., Morris R. V., Lane M. D., Bandfield J. L. and Malin M. C. (2001) Global mapping of Martian hematite mineral deposits: remnants of water-driven processes on early Mars. *J. Geophys. Res.* **106**, 23873–23885.
- Christensen P. R., Wyatt M. B., Glotch T. D., Rogers A. D., Anwar S., Arvidson R. E., Bandfield J. L., Blaney D. L., Budney C., Calvin W. M., Fallacaro A., Ferguson R. L., Gorelick N., Graff T. G., Hamilton V. E., Hayes A. G., Johnson J. R., Knudson A. T., McSween, Jr., H. Y., Mehall G. L., Mehall L. K., Moersch J. E., Morris R. V., Smith M. D., Squyres S. W., Ruff S. W. and Wolff M. J. (2004) Mineralogy at Meridiani Planum from the Mini-TES experiment on the Opportunity Rover. *Science* **306**, 1733–1739.
- Christov C. (2004) Pitzer ion-interaction parameters for Fe(II) and Fe(III) in the quinary {Na + K + Mg + Cl + SO₄ + H₂O} system at $T = 298.15$ K. *J. Chem. Thermodyn.* **36**, 223–235.
- Clark B. C., Morris R. V., McLennan S. M., Gellert R., Jolliff B., Knoll A. H., Squyres S. W., Lowenstein T. K., Ming D. W., Tosca N. J., Yen A., Christensen P. R., Gorevan S., Brückner J., Calvin W., Dreibus G., Farrand W., Klingelhofer G., Waenke H., Zipfel J., Bell, III, J. F., Grotzinger J., McSween H. Y. and Rieder R. (2005) Chemistry and mineralogy of outcrops at Meridiani Planum. *Earth Planet. Sci. Lett.* **240**, 73–94.
- Clegg S. L. and Brimblecombe P. (1990) The solubility and activity coefficient of oxygen in salt solutions and brines. *Geochim. Cosmochim. Acta* **54**, 3315–3328.
- Crowley J. K., Kargel J. S., Marion G. M., Hook S. J., Bridges N. T., Brown A. J. and de Souza Filho C. R. (2006) Mixing and resolution processes affecting evaporite mineral distributions on Earth and Mars. Conference on Sulfates as Recorders of Atmospheric-Fluid-Rock Interactions. *Lunar Planet. Inst.*, Houston, TX. #7056 (abstr.).
- Crowley J. K., Kargel J. S., Marion G. M., Hook S. J., Thomson B. J., de Souza Filho C. R., Bridges N. T., Brown N. T. and Brown A. J. (2007) Detecting reduced zones in oxidized Fe-rich sedimentary rocks: spectral clues to organic matter concentrations? 37th *Lunar Planet. Sci. Conf.*, Houston, TX. #1274 (abstr.).
- Douglas S. (2005) Mineralogical footprints of microbial life. *Am. J. Sci.* **305**, 503–525.
- Drouet C. and Navrotsky A. (2003) Synthesis, characterization, and thermochemistry of K–Na–H₂O jarosites. *Geochim. Cosmochim. Acta* **67**, 2063–2076.
- Feldman W. C., Mellon M. T., Maurice S., Prettyman T. H., Carey J. W., Vaniman D. T., Bish D. L., Fialips C. I., Chipera S. J., Kargel J. S., Elphic R. C., Funsten H. O., Lawrence D. J. and Tokar R. L. (2004) Hydrated states of MgSO₄ at equatorial latitudes on Mars. *Geophys. Res. Lett.* **31**(16), L16702. doi:10.1029/2004GL020181.
- Fernandez-Remolar D., Gomez-Elvira J., Gomez F., Sebastian E., Martiin J., Manfredi J. A., Torres J., Gonzalez Kesler C. and Amils R. (2004) The Tinto River, an extreme acidic environment under control of iron, as an analog of the Terra Meridiani hematite site of Mars. *Plant. Space Sci.* **52**, 239–248.
- Fernandez-Remolar D. C., Morris R. V., Gruener J. E., Amils R. and Knoll A. H. (2005) The Rio Tinto Basin, Spain: mineralogy, sedimentary geobiology, and implications for interpretation of outcrop rocks at Meridiani Planum, Mars. *Earth Planet. Sci. Lett.* **240**, 149–167.
- Fernandez-Remolar D. C., Prieto-Ballesteros O., Rodriguez N., Gomez F., Amils R., Gomez-Elvira J. and Stoker C. (in press) Underground habitats found in the Rio Tinto Basin: an approach to Mars subsurface life exploration. *Astrobiology*.
- Gendrin A., Mangold N., Bibring J.-P., Langevin Y., Gondet B., Poulet F., Bonello G., Quantin C., Mustard J., Arvidson R. and LeMouelic S. (2005) Sulfates in Martian layered terrains: the OMEGA/Mars Express view. *Science* **307**, 1587–1591.
- Glotch T. D. and Christensen P. R. (2005) Geologic and mineralogic mapping of Aram Chaos: evidence for a water-rich history. *J. Geophys. Res.* **110**, E09006.
- Glotch T. D. and Rogers A. D. (2007) Evidence for aqueous deposition of hematite and sulfate-rich light-toned deposits in Aureum and Iani Chaos, Mars. *J. Geophys. Res.* **112**, E06001.
- Golden D. C., Ming D. W., Morris R. V. and Mertzman S. A. (2005) Laboratory-simulated acid-sulfate weathering of basaltic materials: implications for formation of sulfates at Meridiani Planum and Gusev Crater, Mars. *J. Geophys. Res.* **110**, E12S07. doi:10.1029/2005JE002451.
- Hardie L. A. and Eugster H. P. (1970) The evolution of closed-basin brines. *Mineral. Soc. Am. Spec. Publ.* **3**, 273–290.
- Hemingway, B.S., Seal, R.R., II, Chou I-M. (2002). Thermodynamic data for modeling acid mine drainage problems: compilation and estimation of data for selected soluble iron-sulfate minerals. Open-File Report 02-161, U.S. Geol. Surv., Reston, VA.
- Herkenhoff K. E., Squyres S. W., Arvidson R., Bass D. S., Bell, III, J. F., Bertelsen P., Ehlmann B. L., Farrand W., Gaddis L., Greeley R., Grotzinger J., Hayes A. G., Hviid S. F., Johnson J. R., Jolliff B., Kinch K. M., Knoll A. H., Madsen M. B., Maki J. N., McLennan S. M., McSween H. Y., Ming D. W., Rice, Jr., J. W., Richter L., Sims M., Smith P. H., Soderblom L. A., Spanovich N., Sullivan R., Thompson S., Wdowiak T., Weitz C. and Whelley P. (2004) Evidence from Opportunity's microscopic imager for water on Meridiani Planum. *Science* **306**, 1727–1730.
- Hogenboom D. L., Kargel J. S., Ganasan J. and Lee L. (1995) Magnesium sulfate–water to 400 MPa using a novel piezometer: densities, phase equilibria, and planetological implications. *Icarus* **115**, 258–277.
- ICT (1928) International Critical Tables, McGraw-Hill, New York.
- Jambor J. L., Nordstrom D. K. and Alpers C. N. (2000) Metal-sulfate salts from sulfide mineral oxidation. In *Sulfate Minerals: Crystallography, Geochemistry, and Environmental Significance. Reviews in Mineralogy and Geochemistry*, vol. 40 (eds. C. N. Alpers, J. L. Jambor and D. K. Nordstrom). Mineral. Soc. Am., Washington, DC, pp. 305–350.
- Jolliff B.L., McLennan S.M. and the Athena Science Team. (2006) Evidence for water at Meridiani. *Elements* **2**, 163–167.
- Kargel J. S., Delmelle P. and Nash D. B. (1999) Volcanogenic sulfur on Earth and Io: composition and spectroscopy. *Icarus* **142**, 249–280.
- Kargel J. S. (2004a) *Mars: A Warmer, Wetter Planet*. Praxis-Springer, New York.
- Kargel J. S. (2004b) Proof of Water, Hints of Life?. *Science* **306**, 1689–1691.
- Kargel J. S. and Marion G. M. (2004) Mars as a salt-, acid-, and gas-hydrate world. 35th *Lunar Planet. Sci. Conf.*, Houston, TX. #1965 (abstr.).

- Kargel, J. S., Furfaro, R., Prieto-Ballesteros, O., Rodriguez J. A. P., Montgomery D. R., Gillespie A. R., Marion G. M. and Wood, S.E., (in press). Martian hydrogeology sustained by thermally insulating gas and salt hydrates. *Geology*.
- King P. L., Lescinsky D. T. and Nesbitt H. W. (2004) The composition and evolution of primordial solutions on Mars, with application to other planetary bodies. *Geochim. Cosmochim. Acta* **68**, 4993–5008.
- Klingelhöfer G., Morris R. V., Bernhardt B., Schröder C., Rodionov D. S., de Souza, Jr., P. A., Yen A., Gellert R., Evlanov E. N., Zubkov B., Foh J., Bonnes U., Kankeleit E., Gütllich P., Ming D. W., Renz F., Wdowiak T., Squyres S. W. and Arvidson R. E. (2004) Jarosite and hematite at Meridiani Planum from Opportunity's Mössbauer Spectrometer. *Science* **306**, 1740–1745.
- Krumgalz B. S., Starinsky A. and Pitzer K. S. (1999) Ion-interaction approach: pressure effect on the solubility of some minerals in submarine brines and seawater. *J. Soln. Chem.* **28**, 667–692.
- Lane M. D., Darby Dyar M. and Bishop J. L. (2004) Spectroscopic evidence for hydrous iron sulfate in the Martian soil. *Geophys. Res. Letters*. **31**, L19702. doi:10.1029/2004GL021231.
- Langevin Y., Poulet F., Bibring J.-P. and Gondet B. (2005) Sulfates in the north polar regions of Mars detected by OMEGA/Mars Express. *Science* **307**, 1584–1586.
- W. F. Linke (Ed.) (1958) Solubilities: Inorganic and Metal-Organic Compounds. A–I. A Compilation of Solubility Data from the Periodical Literature, fourth ed, vol. 1, Am. Chem. Soc., Washington, D.C.
- Majzlan J., Grevel K. D. and Navrotsky A. (2003) Thermodynamics of Fe oxides: Part II. Enthalpies of formation and relative stability of goethite (α -FeOOH), lepidocrocite (γ -FeOOH), and maghemite (γ -Fe₂O₃). *Am. Mineral.* **88**, 855–859.
- Majzlan J., Navrotsky A., McCleskey R. B. and Alpers C. N. (2006) Thermodynamic properties and crystal structure refinement of ferricopiapite, coquimbite, rhomboclase, and Fe₂(SO₄)₃(H₂O)₅. *European J. Mineral.* **18**, 175–186.
- Majzlan J., Navrotsky A. and Schwertmann U. (2004) Thermodynamics of iron oxides: Part III. Enthalpies of formation and stability of ferrihydrite (\sim Fe(OH)₃), schwertmannite (\sim FeO(OH)_{3/4}(SO₄)_{1/8}), and e-Fe₂O₃. *Geochim. Cosmochim. Acta* **68**, 1049–1059.
- Majzlan J., Navrotsky A., Stevens R., Donaldson M., Woodfield B. F. and Boerio-Goates J. (2005) Thermodynamics of monoclinic Fe₂(SO₄)₃. *J. Chem. Thermodynamics*. **37**, 802–809.
- Marion G. M. (2001) Carbonate mineral solubility at low temperatures in the Na–K–Mg–Ca–H–Cl–SO₄–OH–HCO₃–CO₃–CO₂–H₂O system. *Geochim. Cosmochim. Acta* **65**, 1883–1896.
- Marion G. M. (2002) A molal-based model for strong acid chemistry at low temperatures (<200 to 298 K). *Geochim. Cosmochim. Acta* **66**, 2499–2516.
- Marion G. M. (2007) Adapting molar data (without density) for molal models. *Comput. Geosci.* **33**, 829–834.
- Marion G. M., Catling D. C. and Kargel J. S. (2003) Modeling aqueous ferrous iron chemistry at low temperatures with application to Mars. *Geochim. Cosmochim. Acta* **67**, 4251–4266.
- Marion G. M., Catling D. C. and Kargel J. S. (2006a) Modeling gas hydrate equilibria in electrolyte solutions. *CALHAD*. **30**, 248–259.
- Marion G. M. and Farren R. E. (1999) Mineral solubilities in the Na–K–Mg–Ca–Cl–SO₄–H₂O system: a re-evaluation of the sulfate chemistry in the Spencer–Møller–Weare model. *Geochim. Cosmochim. Acta* **63**, 1305–1318.
- Marion G. M. and Kargel J. S. (2005) Stability of magnesium sulfate minerals in Martian environments. *36th Lunar Planet. Sci. Conf.*, Houston, TX. #2290 (abstr.).
- Marion G. M. and Kargel J. S. (in press) Cold Aqueous Planetary Geochemistry with FREZCHEM: From Modeling to the Search for Life at the Limits. Springer, Berlin.
- Marion G. M., Kargel J. S. and Catling D. C. (2006b) Modeling ferrous-ferric iron chemistry with application to Martian surface geochemistry. *37th Lunar Planet. Sci. Conf.*, Houston, TX. #1898 (abstr.).
- Marion G. M., Kargel J. S., Catling D. C. and Jakubowski S. D. (2005) Effects of pressure on aqueous chemical equilibria at subzero temperatures with applications to Europa. *Geochim. Cosmochim. Acta* **69**, 259–274.
- Marion G. M., Mironenko M. V. and Roberts M. W. (2006c) FREZCHEM: an aqueous geochemical model for Mars. Amer. Geophys. Union Annual Meeting, San Francisco, CA. #768 (abstr.).
- McLennan S. M., Bell J. F., Calvin W. M., Christensen P. R., Clark B. C., de Souza P. A., Farmer J., Farrand W. H., Fike D. A., Gellert R., Ghosh A., Glotch T. D., Grotzinger J. P., Hahn B., Herkenhoff K. E., Hurowitz J. A., Johnson J. R., Johnson S. S., Jolliff B., Klingelhofner G., Knoll A. H., Learner Z., Malin M. C., McSween H. Y., Pockock J., Ruff S. W., Soderblom L. A., Squyres S. W., Tosca N. J., Watters W. A., Wyatt M. B. and Yen A. (2005) Provenance and diagenesis of the evaporite-bearing Burns formation, Meridiani Planum, Mars. *Earth Planet. Sci. Lett.* **240**, 95–121.
- McSween, Jr., H. Y. (2006) Water on Mars. *Elements*. **2**, 135–137.
- Millero F. J. (2001) *Physical Chemistry of Natural Waters*. Wiley-Interscience, New York.
- Ming D. W., Mittlefehldt D. W., Morris R. V., Golden D. C., Gellert R., Yen A., Clark B. C., Squyres S. W., Farrand W. H., Ruff S. W., Arvidson R. E., Klingelhöfer G., McSween H. Y., Rodionov D. S., Schröder C., de Souza, Jr., P. A. and Wang A. (2006) Geochemical and mineralogical indicators for aqueous processes in the Columbia Hills of Gusev Crater, Mars. *J. Geophys. Res.* **111**, E02S12. doi:10.1029/2005JE002560.
- Montgomery D. and Gillespie A. (2005) Formation of Martian outflow channels by catastrophic dewatering of evaporite deposits. *Geol.* **33**, 625–628.
- Morris R. V., Klingelhöfer G., Bernhardt B., Schröder C., Rodionov D. S., de Souza, Jr., P. A., Yen A., Gellert R., Evlanov E. N., Foh J., Kankeleit E., Gütllich P., Ming D. W., Renz F., Wdowiak T., Squyres S. W. and Arvidson R. E. (2004) Mineralogy at Gusev Crater from the Mössbauer spectrometer on the Spirit Rover. *Science* **305**, 833–836.
- Morris R. V., Klingelhöfer G., Schröder C., Rodionov D. S., Yen A., Ming D. W., de Souza, Jr., P. A., Fleischer I., Wdowiak T., Gellert R., Bernhardt B., Evlanov E. N., Zubkov B., Foh J., Bonnes U., Kankeleit E., Gütllich P., Renz F., Squyres S. W. and Arvidson R. E. (2006) Mössbauer mineralogy of rock, soil, and dust at Gusev Crater, Mars: Spirit's journey through weakly altered olivine basalt on the plains and pervasively altered basalt in the Columbia Hills. *J. Geophys. Res.* **111**, E02S13. doi:10.1029/2005JE002584.
- Morse J. W. and Marion G. M. (1999) The role of carbonates in the evolution of early Martian oceans. *Am. J. Sci.* **299**, 738–761.
- Navrotsky A., Lázár Forray F. and Drouet C. (2005) Jarosite stability on Mars. *Icarus*. **176**, 250–253.
- Nordstrom D. K. and Munoz J. L. (1994) *Geochemical Thermodynamics*, second ed. Blackwell Science Publications, Boston.
- Peterson R. C. and Wang R. (2006) Crystal molds on Mars: melting of a possible new mineral species to create Martian chaotic terrain. *Geology* **34**, 957–960.
- Pitzer K. S. (1991) Ion interaction approach: theory and data correlation. In *Activity Coefficients in Electrolyte Solutions*, Second ed. CRC Press, Boca Raton, pp. 75–153.

- Pitzer K. S. (1995) *Thermodynamics*, third ed. McGraw-Hill, New York.
- Plummer L. N., Parkhurst D. L., Fleming G. W. and Dunkle S. A. (1988) A computer program incorporating Pitzer's equations for calculation of geochemical reactions in brines. *U.S. Geol. Surv. Water Res. Inv. Rep.*, 88–4153.
- Reardon E. J. (1988) Ion interaction parameters for AlSO_4 and application to the prediction of metal sulfate solubilities in binary salt systems. *J. Phys. Chem.* **92**, 6426–6431.
- Robie R. A. and Hemingway B. S. (1995) *Thermodynamic Properties of Minerals and Related Substances at 298.15 K and 1 bar (10^5 Pascals) Pressure and at Higher Temperatures*. U.S. Geol. Survey Bull. 2131. U.S. Gov. Print. Office, Washington, D.C.
- Rodriguez J. A. P., Kargel J. S., Crown D. A., Bleamaster, III, L. F., Tanaka K. L., Baker V., Miyamoto H., Dohm J. M., Sasaki S. and Komatsu G. (2006) Headward growth of chasmata by volatile outbursts, collapse, and drainage: evidence from Ganges Chaos, Mars. *Geophy. Res. Lett.* **33**(18), L18203.
- Schwertmann U., Friedl J. and Stanjek H. (1999) From Fe(III) ions to ferrihydrite and then to hematite. *Science* **209**, 215–223.
- Squyres S. W., Grotzinger J. P., Arvidson R. E., Bell, III, J. F., Calvin W., Christensen P. R., Clark B. C., Crisp J. A., Farrand W. H., Herkenhoff K. E., Johnson J. R., Klingelhöfer G., Knoll A. H., McLennan S. M., McSween, Jr., H. Y., Morris R. V., Rice, Jr., J. W., Rieder R. and Soderblom L. A. (2004) In situ evidence for an ancient aqueous environment at Meridiani Planum, Mars. *Science* **306**, 1709–1714.
- Squyres S. W., Knoll A. H., Arvidson R. E., Clark B. C., Grotzinger J. P., Jolliff B. L., McLennan S. M., Tosca N., Bell, III, J. F., Calvin W. M., Farrand W. H., Glotch T. D., Golombek M. P., Herkenhoff K. E., Johnson J. R., Klingelhöfer G., McSween H. Y. and Yen A. S. (2006) Two years at Meridiani Planum: results from the Opportunity Rover. *Science* **313**, 1403–1407.
- Tosca N. J. and McLennan S. M. (2006) Chemical divides and evaporitic assemblages on Mars. *Earth Planet. Sci. Lett.* **241**, 21–31.
- Tosca N. J., McLennan S. M., Clark B. C., Grotzinger J. P., Hurowitz J. A., Knoll A. H., Schröder C. and Squyres S. W. (2005) Geochemical modeling of evaporation processes on Mars: insight from the sedimentary record at Meridiani Planum. *Earth Planet. Sci. Lett.* **240**, 122–148.
- Tosca N. J., Smirnov A. and McLennan S. M. (2007) Application of the Pitzer ion interaction model to isopiestic data for the $\text{Fe}_2(\text{SO}_4)_3\text{-H}_2\text{SO}_4\text{-H}_2\text{O}$ system at 298.15 and 323.15 K. *Geochim. Cosmochim. Acta* **71**, 2680–2698.
- Wang A., Korotev R. L., Jolliff B. L., Haskin L. A., Crumpler L., Farrand W. H., Herkenhoff K. E., de Souza P., Kusack A. G. and Hurowitz J. A. (2006) Evidence of phyllosilicates in Woolly Patch, an altered rock encountered at West Spur, Columbia Hills, by the Spirit rover in Gusev Crater, Mars. *J. Geophys. Res.* **111**(E2), E02S16. doi:10.1029/2005JE002516.

Associate editor: Robert H. Byrne